The present work was submitted to the Faculty of Engineering

Unmanned Aerial Vehicle structural design

Bachelor Thesis

by

Enkh-Amgalan Baigal

Supervisor 1 / Examiner 1	**Prof. Dr. P. E. Sungchil Lee**
Supervisor 2 / Examiner 2	**Prof. Dr.-Ing Thomas Hollenberg**

Ulaanbaatar/Nalaikh, May 8th, 2023

GERMAN - MONGOLIAN INSTITUTE FOR RESOURCES AND TECHNOLOGY

Acknowledgments

Firstly, I would like to express my deepest gratitude and warmest thanks to my supervisors, Prof. Sungchil Lee and Prof. Dr.-Ing. Tomas Hollenberg for making my bachelor thesis study possible. Their guidance, advice, and motivation carried me through my entire thesis writing phase. They were the primary source of my willingness to make this thesis work a unique experience in the engineering field.

I would also like to give special thanks to the German Mongolian Institute for Resources and Technology for their support.

Finally, I would like to thank my family and friends for their support throughout the difficulties, ups, and downs. Their everlasting support made me make it through the entire writing process.

GERMAN - MONGOLIAN INSTITUTE FOR RESOURCES AND TECHNOLOGY

Table of Contents

Statutory Declaration

Baigal, Enkhamgalan	15614548153614
Last Name, First Name	Student ID Number

I hereby affirm in lieu of an oath that I provided the submitted bachelor thesis

"UNMANNED AERIAL VEHICLE STRUCTURAL DESIGN"

I did not use any sources other than those stated. In case that the work is additionally submitted on a data medium, I declare that the written and the electronic form are completely identical. The work was not submitted in the same or similar form to any examination authority.

5/10/2023	
Place, Date	Signature

List of Abbreviations

ISA- International Standart Artmosphere

UAV- Unmanned Aerial Vehicle

NACA- National Advisory Committee for Aeronautics

NASA- National Aeronautics and Space Administration

CFD- Computational Fluid Dynamics

LOS- Line of Sight

M.A.C- Mean Aerodynamic Chord

A.R- Aspect Ratio

RANS- The Reynolds-Averaged Navier Stokes

Re- Reynolds Number

C_l- Coefficient of Lift

C_d- Coefficient of drag

List of Tables and Charts

List of Figures

Figure 28. NACA 63(4)-221 and NACA 63(4)-421 velocity contour

Figure 29. NACA 63(4)-221 and NACA 63(4)-421 pressure contour

Figure 30. NACA 63(4)-421 a0 pressure contour Figure 31. NACA 63(4)-421 a0 velocity contour

List of Equations

Abstract

This study focuses on the design, analysis, and selection of an airfoil for a heavy-lifting unmanned aerial vehicle (UAV) with the aim of achieving optimal aerodynamic performance. The UAV is intended for civilian and reconnaissance applications and must be capable of carrying a maximum take-off weight of 450 kg while operating at an altitude of 4000 meters. As such, the airfoil design must provide high lift-to-drag ratios and fulfill specific performance criteria to ensure efficient and reliable operation under the designated conditions.

Through rigorous computational fluid dynamics (CFD) simulations and a comprehensive assessment of various airfoil candidates, the NACA 634421 airfoil was identified as the most suitable choice for this application. At a 10-degree angle of attack, this airfoil exhibits favorable aerodynamic characteristics, meeting the required lift coefficient and demonstrating a satisfactory lift-to-drag ratio. The study delves into the effects of airfoil geometry, camber, and flow separation on lift generation and drag reduction, emphasizing the critical role of airfoil selection in the overall performance and efficiency of the UAV.

Additionally, this research explores the relationship between pressure and velocity contours and their impact on the airfoil's aerodynamic properties. The analysis highlights the importance of understanding flow separation and its consequences on lift and drag, providing valuable insights for future airfoil optimization.

The results and recommendations presented in this study offer a solid foundation for the development of heavy-lifting UAVs and contribute to the growing body of knowledge in the field of airfoil design. Furthermore, the study identifies areas for future research, including experimental validation through wind tunnel testing and the use of more sophisticated simulation tools to overcome the limitations of the current computational approach, such as the low y-plus value encountered in the CFD simulations.

In conclusion, this research demonstrates the significance of selecting an appropriate airfoil design for heavy-lifting UAVs, contributing to the advancement of UAV technology and its potential applications in civilian and reconnaissance operations.

1 Introduction

Unmanned aerial vehicles (UAVs), or drones, have experienced rapid growth and adoption across various industries and sectors, offering versatile capabilities in surveillance, data collection, and payload transportation. Heavy-lift drones, capable of carrying substantial payloads, have garnered significant interest for their potential to address the challenges faced in high-altitude civilian reconnaissance missions. The UAV comprises various components, such as the airfoil, fuselage, propulsion system, payload compartment, and others, that work together to ensure optimal performance and functionality. This thesis focuses on the UAV airfoil design and optimization of a heavy-lift drone with a maximum takeoff weight of 450 kg, capable of operating at altitudes up to 4000 meters.

The development of a heavy-lift drone suitable for high-altitude operation necessitates a thorough understanding of aerodynamics, as the airfoil design plays a critical role in determining the drone's lift, drag, and overall performance. The selection and optimization of airfoils must consider factors such as lift-to-drag ratio, stall characteristics, and Reynolds number to ensure efficiency and stability in the intended operational environment.

The primary objectives of this thesis are to Investigate the fundamental principles of airfoil design and their implications for heavy-lift drones operating at high altitudes, with a focus on lift generation, drag reduction, and stall behavior. Analyze the performance of existing airfoil profiles, such as NACA and custom designs, to identify the most suitable candidates for the heavy-lift drone's operational requirements. Develop a systematic approach for airfoil optimization, utilizing computational fluid dynamics (CFD) simulations and wind tunnel testing to refine the selected airfoil profile and maximize the drone's aerodynamic performance. Examine the influence of design parameters such as camber, thickness, and chord length on the airfoil's performance and their implications for the overall drone design.

By addressing these objectives, this thesis aims to provide valuable insights and guidance for the development of airfoil designs tailored for heavy-lift drones capable of operating at high altitudes in civilian reconnaissance applications.

2 State of the Art

2.1 Design principle

Developing the design of an unmanned aerial vehicle (UAV) is a complex process that requires a multidisciplinary approach. The process begins with defining and characterizing the mission requirements such as desired payload, endurance, cruise and maximum altitude, and also cruising velocity. After the initial stage, the designer of the UAV narrows down potential aircraft airframe types through an initial sizing process which is based on similar aircraft which also has similar mission range. Subsequently, the designer must investigate the aerodynamic efficiency and characteristics of the narrowed-down potential airframe/structure configurations. Moreover, designers must investigate if an established aerodynamic geometrical layout offers enough space for all necessary and required systems, and also calculate expected structural responses based on anticipated load. Lastly, the selection of a suitable engine that meets the thrust requirement. However, as said above this study will investigate aerodynamic airfoil structure efficiency. (1)

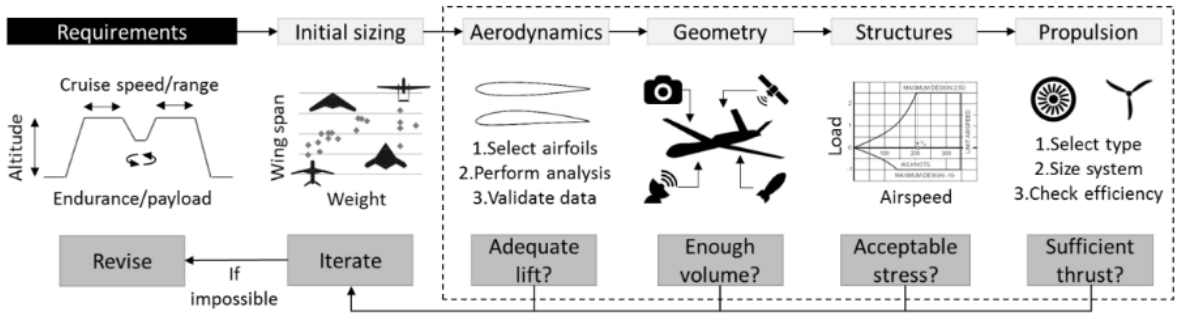

Figure 1. General design process (Athanasios Papageorgiou)

Efficiency is the key consideration in UAV design, the goal being to create solutions that are both airworthy and controllable while achieving satisfactory or optimal performance in a given mission type and environment. UAV designers must optimize various factors while designing airframes such as initial airfoil or wing design, aerodynamic efficiency, and propulsion efficiency to fulfill these goals. The geometry of the airframe including wings, airfoil thickness, and camber percentage must be optimized in order to reduce the drag and increase the lift. Computational fluid dynamics simulation can be utilized to refine the design and assess the given design in different environments and configurations. A wind tunnel experiment is recommended however the university currently does not possess a wind tunnel to test the design. Thus, a computational method is recommended.

Ultimately, the success of the design is affected by a number of factors, and designers must interplay all factors. Including even regulatory and operational constraints, depending on the operator's mission type may necessitate the integration of sophisticated sensors and systems. Payload, system requirements, and demand for modifications to the airframe.

2.2 Falco UAV Airfoil design and testing at Galileo Avionica

The paper presents an in-depth analysis of UAV performance requirements for FALCO UAV, which is developed to be used for aerial surveillance systems for both military and civil application. The UAV was initially designed for medium or long endurance, all-weather capability, rapid deployment, and 24-hour availability. The article also provides further information about major operational requirements STOL characteristics, the capability to operate from unprepared surfaces or naval vessels, and maneuverability. (2)

The major requirements:

- Medium / Long endurance
- All weather conditions
- Logistic flexibility

In terms of performance requirements for FALCO UAV, the paper has provided various specifications due to the diversity of mission types which the UAV has to perform. Including reconnaissance missions to disaster management and telecommunications. With 500 kg as its maximum takeoff weight, it has to meet specific performance requirements.

The performance requirements:

- Stall speed (EAS) 30 m/s
- Initial rate of climb 6.5 m/s
- Maximum ceiling 6000 m (20000 ft)
- Cruise speed 45 m/s
- Endurance varied from mission type
- Line of sight range > 150 km (81 nm) (2)

With many factors to consider in terms of performance requirement capabilities set by designers. One such factor was stalling speed requirements were primarily related to take-off and landing performance. However, due to the EASE “Equivalent Energy” classification of UAVs stall speed was related to applicable airworthiness criteria for civilian certification of the air vehicle. This highlights the importance of the stall speed of UAV ensuring its reliable and safe operating conditions.

Furthermore, another key factor to take into consideration was the initial rate of the climb which was heavily influenced by the maximum ceiling requirements. The maximum ceiling height is particularly important for military applications where silent and safe flying is crucial above hostile environments. However, it also raises the problem of the safety and reliability of the UAV while overflying populated areas in civilian missions. Such as engine malfunction over the populated

area for single-engine UAVs. The capability of flying at certain altitudes is both indirectly and directly related to maximum range criteria due to the curvature of the earth affecting the direct line of sight (LOS) distance.

The paper also emphasized the critical consideration of Cruise speed. Particularly for operation requirements involving time to reach a designated area or overflown square km per flight hour. However, it is worth mentioning that propeller-driven, piston-engine, lightweight UAVs optimized for long-endurance flight at high altitudes typically have low speeds compared to conventional aircraft. As a result, the cruising speed requirements include stall speed and maximum ceiling requirements. This type of UAV has approximately 80-90 knots true airspeed (TAS). Lastly, a comprehensive understanding of these factors is crucial for the successful operation of UAVs in various applications. (2)

Also, this literature discusses the requirements for designing a wing section for a UAV. The crucial part of the design includes

- High L/D ratios for the aircraft due to its medium to long endurance.
- A high ceiling parameter is necessary for a high ceiling performance: M2CLmax.
- A high initial rate of climb: CL3/2/CD.
- High wing loadings for all-weather capability.
- High CL max (maximum lift coefficient) for STOL (short take-off and landing).

Furthermore, aerodynamic parameters are both directly and indirectly influenced by geometric shape requirements are the following:

- High specific structural resistance
- Redundant control surfaces
- Small sensitivity to surface roughness (imperfection and dirt debris)
- High thickness for fuel volume inside the wing structure. (2)

Furthermore, the paper delves into the historical UAV designs which have had similar Mean Aerodynamic Chords around 0.6 meters regardless of weight and designation. However, the wing designs are differentiated mainly by aspect ratio. UAVs have higher wing loading than general aviation aircraft of the same size and weight. But to achieve optimal ceiling and power parameters, it is typically more desirable to minimize the induced drag of a wing by maximizing its aspect ratio. Rather than opting for low loaded low aspect ratio wings which can result in decreasing overall performance. Also, due to the physical limits of the airfoil, the drag cannot be reduced below a certain limit, especially in low Reynold number scenarios. Therefore, designing a wing section with a relatively high aspect ratio (preferably >10) and a highly loaded airfoil can produce satisfying performance. The approach of this kind reduces the overall drag despite airfoil drags by minimizing the wing surface area with a smaller span and chord. The primary design goal is to minimize the drag as much as possible while maintaining the high (fixed) lift coefficient value.

Air Vehicle	*T/O weight [kg]*	*Wing surf. [m^2]*	*Wing span [m]*	*AR*	*M.A.C. [m]*
Meteor Mirach 26	230	2.94	4.50	6.89	0.669
Kentron Seeker	240	4.24	7.00	11.50	0.628
RUAG Ranger	250	3.41	5.47	8.78	0.648
GA-ASI Prowler II	350	4.46	7.31	11.98	0.600
GA-ASI Predator A	1021	11.09	14.85	19.90	0.800
Galileo Avionica Falco	**430**	**4.53**	**7.20**	**11.44**	**0.664**

Table 1. General UAV wing specifications (Source:(2))

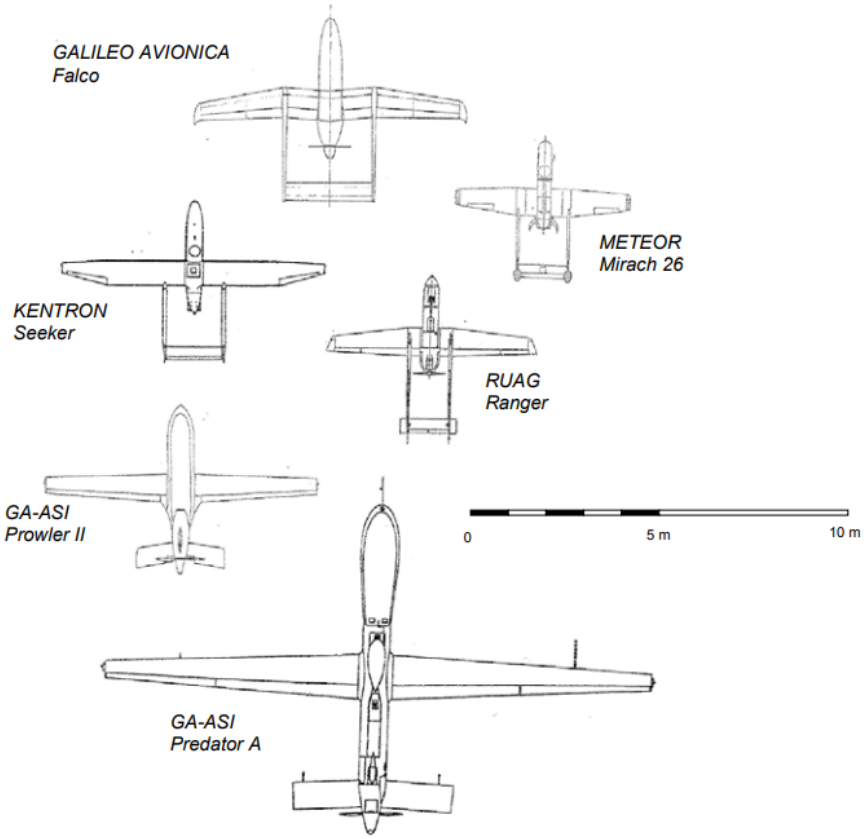

Figure 2. General UAV design (Source:(2))

In the development of unmanned aerial vehicles (UAVs), the initial airfoil design plays a crucial part in achieving satisfactory performance. To this end, Galileo Avionica adopted a multi-point optimization approach. Selection of suitable initial geometry is the first step Galileo Avionica utilized the idea of 2 component airfoil design much similar to those used in Short Take-off and Landing applications. The chosen airfoil type is a 30% chord ratio simple flap rotation for high-lift and rudder control. The main airfoil type was a NACA 6-digit airfoil with 20% thickness, thicker, if possible, selected to better control laminar flow at low Reynolds numbers and thickness also serves another role for providing space for fuel storage and increasing the inertia of main spars.

CFD analysis was then carried out to achieve acceptable drag figures in both cruise and take-off conditions. However, the paper has indicated that it is also important to achieve high lift coefficients in the presence of flow regimes characterized by low Reynolds numbers that could fall below 1.0e06. The two-point optimization design objectives were to minimize drag at CL=0.9 and Re=1.3e06 and for cruise CL=3.0 and Re=1.0e06. (2)

The numerical optimization process was performed at C.I.R.A. based on requirements issued by Galileo Avionica, using a genetic algorithm coupled with a viscous-inviscid interaction method based on a Euler flow solver and an integral boundary layer routine. This method has also been employed by the Israeli Air Force for the design of the Heron UAV.

Throughout the airfoil selection process Galileo Avionica tested 75 different types of airfoils which were generated by an optimization algorithm.

The selected airfoil shows aerodynamic and geometric characteristics of the following features. The blunt nose and high Nose Shape Parameter value for the main element facilitate the smooth movement of the transition point on the upper surfaces. Thereby, preventing high suction points at the leading edge. Moreover, the transition from laminar to turbulent flow is achieved on both design points by using separation bubbles on the main element. Also, the paper suggested that further study was necessary to select the best airfoil. Which is capable of smooth whole geometry, and airfoil curvature.

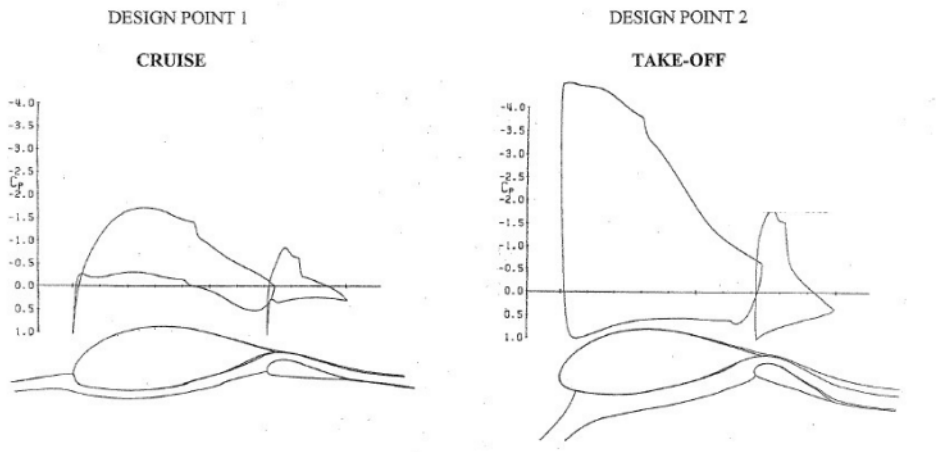

Figure 3. Smooth and transition point surface (Source: directly from (2))

Experiments were performed in a wind tunnel using a real-life-sized wing segment model consisting of a 650mm chord and 600 mm span. Despite the model's low aspect ratio (AR) and strong adverse pressure gradients within the flow field (especially at elevated angles of incidence and flap detection), engineers from Alenia devised a boundary layer suction system along the tunnel walls to maintain two-dimensional airflow. This system operated by drawing in the wall

boundary layer at specific chordwise points due to high-pressure “ejectors” positioned in a passage directly behind the wall

The model was constructed from aluminum, was furnished with an internal balance for rapid force and pitching moment measurements, and more than 100 pressure taps to acquire comprehensive pressure distribution data across the main and flap components of the wing section. A wake rake to gauge drag was positioned roughly 1 chord length downstream.

In this case, wind tunnel testing confirmed the CFD analysis results, although a minor unfavorable impact 10 lift loss was observed in the wing section effectiveness. The maximum lift coefficient lessened as free air stream velocity increased.

In summary, during the main test series, an irregular occurrence of bubble behavior was noted on the primary testing subject. It was an unusual event that bubbles appeared at minimal Reynolds numbers. An investigation using a hot wire anemometer was carried out through examination.

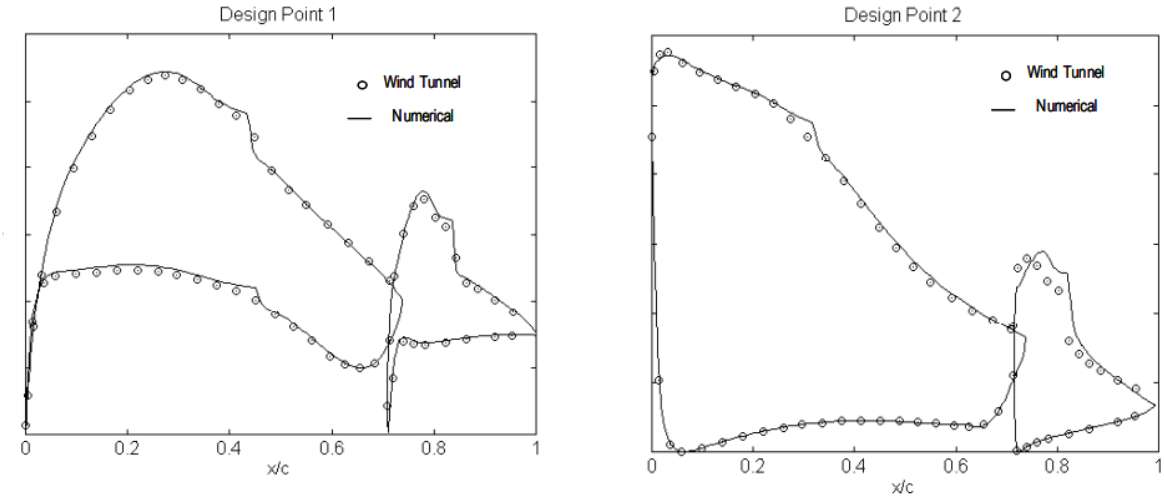

Figure 4. Comparison of pressure distribution (Source:(2))

Drag estimations were obtained by measuring the momentum loss by using a wake rake which we placed along the centerline of the 2D channel. Accurate measurements were only achievable at lower angles of incidence and higher velocities due to the limited sensitivity of pressure transducers connected to the wake rake. The data indicated a notably higher drag compared to CFD predictions, with actual numbers being approximately 20% higher than expected. This result is possibly associated with the previously mentioned increased free stream turbulence level, as laminar bubbles were only observed on the flap suction side during minimum drag experiments.

2.3 Wind tunnel test

The design improvement of Airfoil for flying wing UAV: This article aims to showcase the enhancement of airfoil design for flying wing UAVs while the author collaborated with the University of Putra Malaysia. The design process utilized XFOIL code (an interactive software for designing and analyzing subsonic isolated airfoils) and wing tunnel test outcomes for validation for the simulation outcome. The base airfoil employed was the Eppler E334 (thickness to chord ratio, thickness= 11.93%). Due to the requirement to increase structural durability, the thickness of the chord has to be increased. The ultimate design incorporated the Eppler E334 with a thickness=13.5%. This study primarily focused on how characteristics of aerodynamics would change if the thickness of the airfoil increased.

Figure 5. Flying wing UAV (3)

Simulation: The researcher redesigned the Eppler E334 airfoil by increasing its thickness to 13.5%, creating the Ne334 airfoil. The simulation compares the difference between the given two airfoils' geometry and aerodynamic characteristics of lift, drag, and moment of E334 and Ne334 airfoils at different Reynolds numbers(0.8E6, 0.9E6,1E6, and 1.2E6). The results reveal that the maximum lift coefficient of the Ne334 airfoil increases tremendously for every variation of the Reynolds number at the same angle of attack compared to the original Eppler 334 airfoil.

The author found that the increased thickness of the Ne334 airfoil design did not significantly increase the coefficient of the moment. Which is an essential factor for flying wing airfoils. However, the same results apply to different Reynolds numbers as well. The study also shows that the zero coefficient of the moment is located at an angle of attack close to the maximum lift coefficient. Thus allowing the flying wing UAV to cruise near maximum lift while maintaining a zero pitching moment.

A comparison of the NACA 44-series with the Ne334 airfoil for different thicknesses shows a similar trend: the maximum lift coefficient increases with increasing thickness. The NACA 44-series' maximum lift coefficient continues to increase while that of the Ne334 airfoil reaches its peak at a thickness-to-chord ratio of 17.4. The researchers chose the 13.5% thickness of Ne334

due to its high lift-to-drag coefficient ratio. But it is also important to highlight that increasing the thickness further (higher than 14%) will not provide more lift but will induce more drag and a higher pitching moment.

Researchers have observed that based on the calculations of the pressure coefficient (Cp), the coefficient of lift (Cl) and moment (Cm) can be calculated or obtained at various angles of attack as shown in Table 2.

α	Cl (Wind Tunnel)	Cm (Wind Tunnel)	Cl (XFOIL)	Cm (XFOIL)
-5	-0.7443	-0.0196	-1.3506	0.206
0	0.5162	0.0158	0.3252	-0.033
5	1.1529	0.0247	1.0315	-0.064
10	1.4757	0.0315	1.3935	-0.032
15	1.7268	0.0349	1.5561	0.001
20	1.1078	0.0905	1.3383	-0.02

Table 2. Comparison between' wind tunnel test and XFOIL (Source:(4)*)*

The wind tunnel test results show a high degree of similarity with the simulation of XFOIL. Due to the similarity, it is safe to conclude the Ne334 airfoil is confirmed to have better performance compared to the original E334 airfoil.

Finally, the researcher discovered that with respect to the utilization of the XFOIL program. It is only reliable up to a specific range of angles of attack. Therefore, the researcher has mentioned that caution should be exercised when interpreting the data gathered from the XFOIL program. Moreover, this project did not cover several important aspects of the program such as the boundary layer profile and skin friction coefficient. The author believes that taking all remaining parameters into account could enhance the accuracy of the results.

2.4 UAV Aerodynamics, Flight Stability, and Control.

- **Theoretical Aerodynamics**

Aerodynamic analysis of innovative concepts in UAV design can be carried out using various methodologies, from traditional aerodynamic theories to contemporary computational fluid dynamics (CFD). Thin airfoil theory, an analytical method predicting lift as a function of angle of attack, assumes idealized incompressible inviscid flow. The theory is applicable to airfoils with a thickness not exceeding 12% of the chord (c) at low angles. Max Munk, a German-American mathematician developed the thin airfoil theory which was later refined by British aerodynamicist Hermann Glauert in the 1920s. This theory serves as a solid foundation for modern aerodynamic theories. (5)

Prandtl's lifting line theory is a mathematical model for predicting the lift distribution along the span of a three-dimensional wing Figure 7. In this model, vortex strength varies elliptically along the wingspan, and the decrease in vortex strength is shed as a vortex- sheet from the trailing edge. Lift distribution is derived from wing geometry and freestream conditions, such as air density and flow velocity. Classical lifting theory's modified versions are employed to calculate lift distribution in geometrically or aerodynamically twisted wings.

The vortex panel method is a numerical technique that enables the computation of airfoil lift under the assumption of ideal flow where compressibility and viscosity effects are negligible. This method reconstructs the airfoil surface's shape using a series of vortex panels or line segments arranged to form closed polygons. Vortex sheets simulate the boundary layer around the airfoil. These vortex sheets represent miniature vortices generating circulation and, consequently lift.

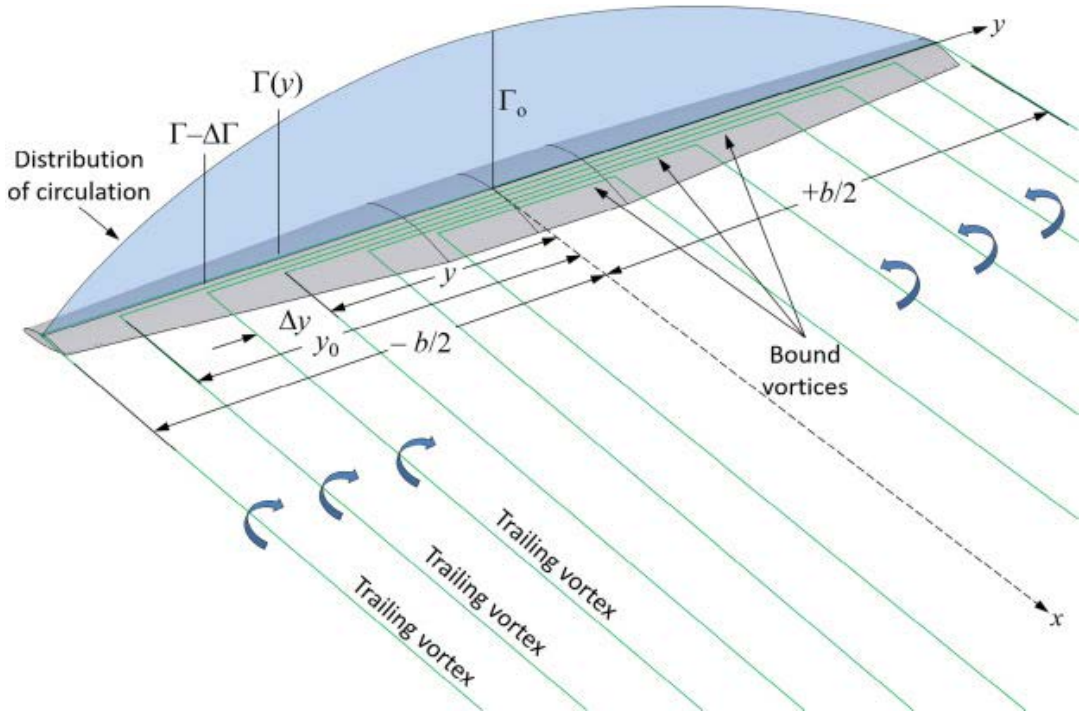

Figure 6. Lifting Line demonstration(6)

- **Flight Regimes and Reynolds number**

The Reynolds number (Re) is a dimensionless quantity representing the ratio of the inertial forces to viscous forces in given flow conditions. This concept, introduced by Osborne Reynolds in 1883 characterizes various flow regimes.

Laminar flow occurs at low Re values where viscous forces are dominant, while turbulent flow occurs at high Re values with inertial forces prevailing. Small UAVs operate within the Re range of 3E4 (3*10^4) and 5E5 (5*10^5). Designing efficient airfoils is crucial for operation at low Re values. For 3E4 Re 7E4, relatively thick airfoils may experience significant hysteresis due to

lift and drag forces caused by laminar separation and transition to turbulent flow. When Re values are below 5E4, laminar separation occurs, and the flow does not transition or reattach to the airfoil surface.

For 7E4 ≤ Re ≤ 2E5, extensive laminar flow over the airfoil surfaces can be achieved, reducing airfoil drag. However, in some airfoils, a laminar separation bubble forms within this flight regime. As Re values exceed 2E5, airfoils become more efficient, the bubble is shorter, and parasite drag diminishes. Large UAVs have a flight regime with Re 3E6. In these high Re values, the laminar boundary layer transitions to turbulence shortly downstream of the wing's leading edge, and laminar separation and separation bubbles do not occur.(5)

- **Airfoil design**

Reducing the operational costs of a UAV can be achieved through airfoil optimization and enhancements in the vehicle's aerodynamic efficiency. Factors to consider when choosing an airfoil for a UAV include a high maximum lift coefficient (climax), high lift-to-drag ratio (cl/cd), high endurance factor (cl^(3/2)/cd), effectiveness at low Re values, low pitching moment coefficient to minimize tail load, mild stall characteristics, resistance to surface roughness due to rain or dust, good flap performance, and minimal airfoil complexity for easier manufacturing.

Airfoils initially designed for high Re values in manned aircraft (3E6 ≤ Re ≤ 6E6) are frequently adapted for UAVs operating in low-Re flight regimes (e.g., 5E5 ≤ Re ≤ 1.5E6). Aerodynamic performance of airfoils in off-design conditions with low Re deteriorates in proportion to the decrease in Re, leading to a lower climax, increased drag, worse cl/cd, and potential lift coefficient (cl) hysteresis behavior as airspeed and Re fluctuates during flight. Hysteresis results from the bursting of the laminar separation bubble at low Re values.

Therefore, when adopting an airfoil for a small UAV, it is crucial to examine the aerodynamic performance and hysteresis of the airfoil in the off-design low-Re flight regimes where the vehicle will operate.(5)

- **Wing geometry**

Induced drag results from wingtip vortices and is an unintended consequence of lift generation by the wing. Wings with a higher aspect ratio (AR) produce less induced drag, improving UAV flight efficiency. Lift generation by a wing depends on various factors, including the airfoil type, wing geometry, air density, airspeed, and angle of attack. UAV designers must evaluate different planform shapes and their corresponding spanwise lift distributions.

Wing planforms for UAVs include rectangular, elliptical, straight tapered, sweptback, sweptback tapered, semi-tapered, forward-swept tapered, delta, double delta, crescent, ogival, blended wing-body, joined, and other shapes. Elliptical planforms are the most efficient, providing constant

lift distribution along the span and minimum induced drag. However, they are challenging to construct. Rectangular planforms are simpler to build but have "idle" wingtips that generate little lift. This platform ensures that wing root stalls before wingtips, maintaining aileron functionality located outboard on the wing.

A practical alternative is a straight wing with tapering towards the tip to enhance spanwise lift distribution. Swept Back tapered planforms display a gradual lift coefficient (cl) increase towards the wingtip, more prominent in delta and double-delta planforms. The tips tend to stall at a lower angle of attack than the wing root, which is undesirable in aircraft as it impairs aileron function and can lead to UAVs dropping a wing or entering difficult-to-recover spins.

To prevent tip stalls in swept back-tapered, delta, and double-delta wings, designers use washout configurations, setting wingtips at a lower angle of incidence than the wing root. Geometric and/or aerodynamic twists are utilized in UAVs to reduce tip vortex strength and associated induced drag, manage stall so the wing root stalls first, and maintain aileron function. Better wing performance is achieved through optimized total twist and elliptical twist distribution along the span.

- **Wing tip devices**

The intensity of wingtip vortices, downwash, and induced drag can be diminished by employing winglets. Winglets effectively increase the wing's aspect ratio (AR). However, their use is often influenced by the aesthetics of the aircraft. Although winglets are designed to limit the tip vortex, it is challenging to demonstrate their effectiveness in real-world situations. Induced drag is inversely proportional to the freestream velocity squared, making vortex drag reduction crucial during slow flight and at high angles of attack and lift coefficient (cl) values. Vortex drag savings are minimal at high speeds, so winglets introduce additional parasite drag at high flight speeds.

The Whitcomb winglet is a specially crafted tip device that draws energy from the wingtip vortex, weakening it and converting energy into forward propulsion. However, the Whitcomb winglet has its limitations. The precise angle of attack for the winglet shifts as the strength of the wingtip vortex varies with flight speed and wing angle of attack, making the winglet efficient only within a narrow range of flight speeds. Despite this, UAVs mostly operate at a single speed, allowing winglet optimization, though extensive research is necessary for optimization.

Most of the lift generated by the winglet acts laterally, which can bend the winglet and add load to the wing structure. This lift generation also creates localized vortices and vortex drag at the winglet tips. Further research is needed to explore the use of winglets in UAV applications. Alternative design options for UAVs include wingtip fences, raked wingtips, non-planar wingtips, upswept tips, Hoerner tips, and tip sails.(5)

2.5 Design of Unmanned Aerial Systems

Aerodynamics is a practical science that deals with the study of air behavior, particularly when it interacts with an object moving through it, such as an unmanned aerial vehicle (UAV). In order to design a UAV aerodynamically, it is important to compute and examine the aerodynamic outcomes of the vehicle. Aerodynamic theories are essential tools for calculating aerodynamic forces and moments (lift, drag, and pitching moment) during the design process. The aerodynamic forces acting on an object in airflow can be determined from the pressure distribution around that object.(7)

The aerodynamic forces of lift and drag on the lifting surface (wing) depends on various factors such as surface angle of attack, geometry, platform area, airspeed, air density, and flow Reynold number. Lift and drag can be calculated using the following formula:

$$L = \frac{1}{2}\rho V^2 S C_l \quad \text{(Eq.1)}$$

L - the lift in Newton equal to the maximum weight of the UAV.

S - the area of the wing, which is computed by multiplying wing's width (or span) by chord length.

V - the horizontal airspeed.

C_l - the coefficient of the lift.

$$D = \frac{1}{2}\rho V^2 S C_d \quad \text{(Eq.2)}$$

D- the drag that would occur throughout the wing space.

C_d- the drag coefficient.

Cl and Cd represent the lift and drag coefficients respectively as said before. The drag coefficient depends on various factors and parameters, especially the UAV configuration. A mathematical expression for the relationship between drag coefficients and lift coefficient are

$$C_d = C_{d_0} + K{C_l}^2 \quad \text{(Eq.3)}$$

K- the variable referred to as the induced drag correction factor.

$$K = \frac{1}{\pi \cdot \varepsilon \cdot AR} \quad \text{(Eq.4)}$$

ε- the Oswald span efficiency factor.

AR- the aspect ratio of the wing.

Airfoil selection or design: A vital aspect of the wing aerodynamic structure design revolves around the determination of its cross-sectional area, or simply airfoil. While a wing is a three-dimensional component, an airfoil is a two-dimensional section. The airfoil section influences the

wing's drag and pitching moment. Wings potentially have constant or non-constant cross-sectional throughout the whole wing. One of the 2 major ways to determine the wing airfoil selection is first airfoil design and second airfoil selection. The design of the airfoil is a complex and time-consuming process and needs expertise in the fundamentals of aerospace design at the graduate level. Also, the expense of wind tunnel testing to verify the initial design is exponential. The author of this book recommends that to select a proper airfoil from the previously designed and published airfoil selections. The most reliable sources are NASA, NACA, and Eppler. (7)

Airfoil selection is part of the overall design process. It begins with a clear statement of flight requirements, as subsonic flight design objectives differ significantly from supersonic flight design objectives. Transonic flight necessitates a specialized airfoil that meets Mach divergence requirements. Designers should also consider requirements, such as airworthiness, structural aerodynamic design, and manufacturability. Considering the aim of this bachelor thesis it is not necessarily important to delve deeper into the manufacturing process.

NACA 4 and 5-digit airfoils exhibit limited efficiency compared to 6-series airfoils. Which demonstrates superior performance and is more prevalent. The 4 and 5-digit airfoils were designed employing simple parabolic and linear shapes without explicitly addressing key aerodynamic design requirements, such as laminar flow and flow separation. Conversely, the 6-digit airfoils were engineered to sustain laminar flow over a substantial portion of the chord, leading to lower drag coefficients in comparison to 4- and 5-digits airfoils. The NACA 6 series airfoils are characterized by five primary digits commencing with the number 6.

NASA recommends several types of airfoil sections including medium-speed MS (1) and low-speed LS (1) series. Analogous to the NACA 4 and 5 digit and 6 series airfoils a broad range of airfoils is available for selection. The most common designations of NASA airfoils are MS (1)-xx yy and LS (1)-xx yy, where xx represents the design lift coefficient, and yy indicates the thickness-to-chord ratio. Both the NASA LS and MS airfoil sections have displayed well-controlled behavior during the wind tunnel testing.

Another favored NASA airfoil is LS (1)-0313 which is often utilized for small vehicles and marginally surpasses the MS series. These airfoils incorporate characteristics of both the original NASA general aviation airfoils and the supercritical airfoils. They demonstrate approximately 40% laminar flow with exceedingly smooth surface finishes and no laminar separation.(7)

A crucial factor in designing airfoil is that Reynolds (Re) number significantly impacts airfoil and wing aerodynamic performance. This factor is of growing importance in the UAV design processes. The majority of UAVs as said before in section 2.2.4 operates at substantially lower Re numbers compared to the three to nine million range where most data are collected. In general, Eppler airfoils are suited for very low Reynolds numbers, and NASA for Low Speed (LS

(1)-xx yy) and Mid Speed (MS (1)-xx yy) for moderate Reynolds. Prior to flight, computationally designed base airfoils must always be subjected to wind tunnel testing.

It is safe to assume that a comprehensive test-verified airfoil section database such as NACA or Eppler is available and rather than designing the wing designer should intend to select an appropriate airfoil from the collection.(7)

Wing design: Wing vertical positioning. During the early stages of wing design one of the crucial parameters is the wing's vertical position relative to the fuselage centerline. This parameter directly affects the design of other aircraft components including the tail and landing gear. There are four primary options for the wing's vertical location including high wing, mid-wing, low wing, and parasol wing. The high-wing configuration offers several advantages such as enhanced lateral stability and increased lift compared to mid and low-wing configurations. Furthermore, the Falco UAV also utilizes a high-wing configuration.(7)

Wing incidence is the angle between the fuselage centerline and the wing chord line at the root. It is sometimes called the wing setting angle. The fuselage centerline lies in the plane of symmetry and typically runs parallel to the cabin floor. The wing must generate the desired lift coefficient during flight. Which corresponds to the airfoil's ideal lift coefficient angle of attack. Most aircraft have wing incidence between 1-4 angle.

Aspect ratio (AR) is defined as the ratio between the wing span (b) and the wing Mean Aerodynamic Chord (MAC or C).

$$AR = \frac{b}{\bar{C}} \quad \text{(Eq.5)}$$

Wing platform area for a rectangular or straight tapered shape is calculated as the span multiplied by mean aerodynamics chords.

$$S = \bar{C} \cdot b \quad \text{(Eq.6)}$$

Wing aspect ratio affects various aircraft features. From an aerodynamic perspective, as AR increases a three-dimensional wing's characteristics become more similar to those of its two-dimensional airfoil section. An increased AR results in higher aircraft maximum lift-to-drag ratio while making the wing structurally heavier. Additionally, a higher AR decreases the effect of the wingtip vortex on the horizontal tail.

A shorter wing is less expensive and less complicated to construct compared to longer wings. As AR increases the aircraft mass moment inertia around the x-axis grows lengthening roll time and reducing maneuverability in a roll. A higher aspect ratio also reduces wing stiffness around the y-axis. The exact AR value should be determined through a comprehensive calculation considering

factors such as requirement performance, stability, and manufacturability. Typical UAV aspect ratios range from 6 to 25.(7)

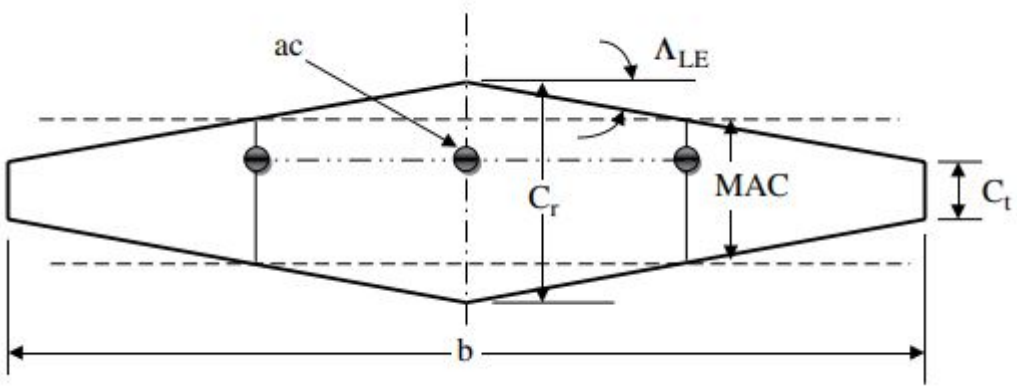

Figure 6. Tapered wing demonstration (7)

Taper ratio

Taper ratio (λ) is defined as the ratio of the chord tip (C_t) to the root of the chord C_r.

$$\lambda = \frac{C_t}{C_r} \text{ (Eq.6)}$$

The taper ratio ranges from 0 to 1 and there are 3 main types of platform designs related to tapering: it includes rectangular, trapezoidal, and delta shapes. A wing with a rectangular platform exhibits a larger downwash angle at the tip compared to the root. As a result, the effective angle of attack at the root, causes the wingtip to stall later than the root. The spanwise lift distribution is far from the highly desirable elliptical shape. Which minimizes induced drag the whole purpose of tapering the platform is mainly to reduce induced drag.

2.6 The CFD Analysis RANS equation review

In Computational Fluid Dynamics (CFD) analysis, The Reynolds-Averaged Navier Stokes (RANS) equations serve as a fundamental tool for accurately predicting fluid flow behavior across a variety of applications. The RANS equations are derived and modified from the Navier-Stokes equations which describe fluid motion. It simply averages the instantaneous flow properties over a specified time period to yield mean flow properties. Moreover, the equation reduces the computational complexity associated with all-time varying turbulent fluctuations.

To effectively model turbulent flow RANS equations requires additional equations of turbulence models. These models introduce necessary equations and closure coefficients to account for turbulent stresses and energy dissipation. Notable RANS-based models include:

1. Spalart-Allmaras Model: A robust and computationally efficient one-equation turbulence model that solves a single transport equation for a modified turbulent

viscosity. This model is particularly apt for aerospace applications, primarily for attached flows and simple separation scenarios.

2. k-epsilon Model: A prevalent two-equation turbulence model that solves two transport equations for turbulent kinetic energy (k) and the dissipation rate (epsilon). This model strikes a balance between computational cost and accuracy for a diverse array of industrial flows, including both external aerodynamics and internal flows.
3. k-omega Model: An alternative two-equation turbulence model that solves transport equations for turbulent kinetic energy (k) and specific dissipation rate (omega). The k-omega model excels in low-Reynolds number and boundary layer flows, demonstrating improved performance in predicting flow separation compared to the k-epsilon model.
4. Shear-Stress Transport (SST) k-omega Model: A sophisticated iteration of the k-omega model that merges the advantages of both k-epsilon and k-omega models. This model exhibits superior performance in predicting adverse pressure gradient flows, flow separation, and the transition between laminar and turbulent flow regimes.

The selection of an appropriate turbulence model is contingent upon the specific application, flow regime, and the desired balance between computational accuracy. In terms of airfoil analysis for UAVs, RANS-based CFD simulations can provide valuable insights into aerodynamic performance. To conclude the following CFD analysis will utilize Shear-Stress Transport (SST) k-omega Model.

2.7 Near-Wall treatment y+ value

In CFD simulations, the near-wall treatment is an essential aspect of accurately capturing flow behavior in the vicinity of solid boundaries, such as the surface of an airfoil. This region typically features complex flow physics, such as boundary layer growth and turbulence. Consequently, understanding and resolving the near-wall region is crucial for obtaining accurate aerodynamic predictions.(8)

The "y+" (y-plus) value is a non-dimensional quantity that characterizes the wall distance in the first grid point from the solid boundary. It is defined as follows:

$$y^+ = \frac{\Delta S \cdot U_{friction}}{\mu \cdot \rho} \quad \text{(Eq.8)}$$

ΔS - the wall spacing of the single mesh (m).

$U_{friction}$- the friction velocity.

μ- the dynamic viscosity (kg/m s).

$$Re_x = \frac{\rho \cdot U \cdot L}{\mu}$$ (Eq.9)

U- the velocity of the medium with respect to the wing.

L- the characteristic length (in this case, the length of the cord.).

ρ- the density of the medium (air for aircraft.).

$$C_f = \frac{0.026}{Re_x^{1/7}}$$ (Eq.10)

C_f- the skin friction coefficient.

$$\tau_{wall} = \frac{C_f \cdot \rho \cdot U^2}{2}$$ (Eq.11)

τ_{wall}- the shear stress at the wall

$$U_{friction} = \sqrt{\frac{\tau_{wall}}{\rho}}$$ (Eq.12)

The y+ value provides critical information on how the computational mesh should be structured to adequately capture the near-wall flow features. The selection of the y+ value depends on the turbulence model and the desired level of fidelity in resolving near-wall flow behavior. In general, there are three regions within the near-wall flow:

Viscous sublayer (y+ < 5): In this region, the flow is predominantly laminar, and the effect of turbulence is minimal. To accurately resolve this layer, a low y+ value is required, and a fine mesh is necessary near the wall.

A buffer layer (5 < y+ < 30): This region serves as a transitional zone between the viscous sublayer and the fully turbulent region. The flow features in this layer are a blend of laminar and turbulent behaviors.

Log-law or fully turbulent region (y+ > 30): This region is dominated by turbulent flow characteristics. In this case, a coarser mesh can be employed without compromising the accuracy of the simulation. When performing CFD simulations for airfoil analysis, it is essential to select an appropriate y+ value based on the chosen turbulence model and desired accuracy. For high-fidelity simulations that require resolving the viscous sublayer, wall-function-based models may not be suitable. Due to their reliance on the use of the logarithmic law of the wall to approximate near-wall flow. Instead, one may opt for low-Reynolds number models or employ more advanced near-wall treatments. Proper near-wall treatment in CFD simulations is guided by the appropriate selection of y+ values. It is one of the most crucial values for obtaining accurate and reliable aerodynamic predictions for airfoil analysis in UAV applications.(8)

A y+ value lower than 1 is often targeted in UAV airfoil simulations because it ensures the accurate resolution of flow characteristics near the airfoil surface, particularly when using low-

Reynolds-number turbulence models. These models attempt to resolve the entire boundary layer, including the viscous sublayer, which is the region close to the wall where the flow is primarily influenced by viscous effects.

UAVs typically operate at lower Reynolds numbers compared to larger aircraft, making the boundary layer behavior and laminar-to-turbulent flow transition more critical to their aerodynamic performance. The resolution of these phenomena requires a very fine mesh near the airfoil surface, which is achieved by maintaining a low y+ value.

When the y+ value is less than 1, the mesh is fine enough to resolve the viscous sublayer accurately, allowing the turbulence model to capture the flow behavior in this region. This leads to a more accurate prediction of lift, drag, and other aerodynamic characteristics that are crucial for UAV design and performance analysis.

However, maintaining a low y+ value can significantly increase computational cost and time due to the increased number of grid points required in the boundary layer mesh. It is essential to balance the need for accurate flow resolution with computational efficiency, considering the specific requirements of the UAV airfoil simulation.(8)

3 Methodology

In this section, the methodology and the calculation involved in airfoil design will be discussed in depth. Given the intricate nature of airfoil design, the examination of the implications of altering airfoil thickness and camber through extensive CFD analysis will be discussed. Accordingly, the selection process will encompass both existing and newly redesigned or enhanced.

Considering the absence of data on redesigned or refigured airfoils, it is essential to address the issue by utilizing Computational Fluid Dynamics (CFD) simulations to accurately analyze and validate the performance of airfoils. The comprehensive analysis approach ensures the selection of the most appropriate airfoil for the intended application. While maintaining the highest standards of aerodynamic efficiency and effectiveness.

3.1 Target requirements

The target requirements for UAV design were predominantly influenced by prevalent industry standards and specifications observes in existing UAV models (Figure circa 2). By selecting a maximum take-off weight, operating altitude, and cruise velocity which corresponds to customer UAV parameters. It ensures the design is well aligned with established norms and performance expectations.

Conforming to these parameters ensures that the UAV design benefits from tried and experimented operating characteristics, while also facilitating compatibility with existing infrastructure and operational systems associated with UAV operations. This methodology streamlines the design process, therefore expanding the operational scale of the UAV into a broader application and mission scenario.

Max take-off weight: A maximum take-off weight of 450 kg was chosen to classify the UAV as an ultralight aircraft. Ultralight aircraft have fewer restrictions and regulatory requirements, making them more convenient for various applications and more accessible to a wider range of users. Additionally maintaining a relatively low weight allows for better fuel efficiency also it increased payload capacity, and improved flight performance.

Operating altitude: An operating altitude of 4,000 m was selected for the UAV to ensure that it can operate effectively in diverse environments and under various atmospheric conditions. A higher operating altitude allows the UAV to avoid obstacles and air traffic more easily, while also providing better surveillance capabilities and enhanced line-of-sight communication. Moreover, operating in higher altitudes typically have more stable and predictable weather conditions. Which results in improved flight performance and reduced risk of turbulence-related issues.

Cruise velocity: A cruise velocity of 36 m/s was chosen to strike a balance between energy efficiency and mission capability. This velocity enables the UAV to cover a considerable distance within a reasonable timeframe, allowing it to effectively perform tasks such as surveillance, data

collection, or delivery. Furthermore, a moderate cruise speed reduces the power consumption, thereby prolonging the flight time and increasing the range of the UAV.

Initial requirement	Values	unit
Max take-off weight	450	kg
Operating altitude	4000	m
Cruise velocity	36	m/s

Table 3. Initial requirements

Dependent parameters	Values	unit
Dynamic viscosity (at 4000m)	1.457E-05	ns/m^2
Kinematic viscosity (at 4000m)	1.779E-05	m^2/s
Reynolds Number	1154362.432	
Chord width	0.65	m
Wing span	12	m
Required Lift	4414.5	N
Density (at 4000m)	0.8194	kg/m^3

Table 4. Dependent variables ISA

From the initial requirements, satisfactory or required coefficients of lift can be calculated by utilizing and rewriting Equation 1.

$$C_l = \frac{2L}{1\rho V^2 S} \quad \text{(Eq.13)}$$

By placing current values of 0.819 kg/m^3, chord length L 0,65m, velocity 36 m/s, and area 7.8 m^2. With the required parameters given the evaluation of the lift coefficient can be conducted. Upon incorporating these values, a lift coefficient (Cl) of 1.065 is obtained. It is crucial to note that this figure represents the minimum lift coefficient the UAV airfoil should produce to ensure its optimal performance. The minimum value serves as a benchmark for the airfoil and sets the initial design phase.

In accordance with the International Standard Atmosphere (ISA) model, several key parameters are derived for an altitude of 4000 meters. The temperature at this altitude is approximately -10.98°C, which is when converted to kelvin equivalent to 262.17 K. Subsequently, the pressure at this altitude is roughly 61,700 Pa (Pascal). To evaluate the dynamic viscosity of air (μ) at this altitude the calculation necessitates the employment of Sutherland's formula (which is a temperature-based equation).(9)

Sutherland's formula follows as:

$$\mu = \mu_0 \left(\frac{T}{T_0}\right)^{\frac{3}{2}} \left(\frac{T_0+S}{T+S}\right) \text{ (Eq.14)}$$

μ- the viscosity (pa s).

T- the Static temperature (262.17K).

μ_0- the Reference viscosity (1.81e-5 pa s).

T_0- the Reference temperature (288.15K).

S- the Sutherland temperature (110.4K).

Replacing all values, now it is safe to initialize evaluation of dynamic viscosity of air at 4000m. is approximately 1.68035e-5 pa s.

Reynolds number calculation is also crucial to determine accuracy. The Reynold number is a dimensionless quantity used to predict turbulence in fluid flow. By utilizing Equation 9 desired value can be calculated.

$$Re = \frac{\rho \cdot U \cdot L}{\mu}$$

U- the velocity of the medium with respect to the wing (36m/s).

L- the characteristic length (in this case, the length of the cord 0.65m.).

ρ- the density of the medium (4000 meters 0.8194).

μ- the dynamic viscosity (1.6803kg/m s)

By replacing the values Reynold's number was calculated as 1141103.374.

3.2 Selection of airfoil shape

Selection of appropriate airfoil for UAV design is a crucial part. Due to the high impact on UAVs performance, efficiency, and broad mission types. There are numerous airfoil profiles available each with unique characteristics which may be suitable for specific UAV applications. As discussed in the literature review of all the airfoil types NACA 6-digit airfoil was chosen. Due to its exhibition of higher efficiency compared to 4- and 5-series airfoils. Also, Galileo Avionica's Falco UAV, which has similar operational characteristics to the current UAV requires performance characteristics and utilizes a NACA 6-digit series airfoil. Furthermore, the selection considered a minimum of 20% airfoil thickness in order to achieve more increased structural capability.

From calculation 1, the minimal required lift coefficient has been found. Thus, it is appropriate to select an airfoil that can outperform the already-found lift coefficient (1.065). Moreover, the high lift and drag ratio is crucial since it indicates a more efficient aircraft capable of longer ranges or endurance for the same fuel consumption. The following airfoils were initially chosen due to their high list coefficients and lift-to-drag ratios. The data on these airfoils were taken from NACA's official experiment report. However, the experiments were done in a high

Reynold number environment 3 million to be precise also test subject chord length was 24 inches (0.6096 meters). Due to the changes further CFD analysis will be done. The chosen potential airfoil designs were NACA 63(4)-421, NACA 63(4)-221, NACA 65(4)-421, and NACA 65(4)-421a5.

The NACA 63(4)-421 airfoil allows for better control over the pressure distribution, providing a more extensive range of desired aerodynamic properties. The NACA 63(4)-421 airfoil is a member of the NACA 6-series family of airfoils, characterized by its specific camber and thickness distribution. This particular airfoil features a maximum thickness of 21% located at 34.8% of the chord length from the leading edge. In addition, it has a maximum camber of 2.2% situated at 50% of the chord.

NACA 63(4)-421 airfoil exhibits favorable aerodynamic characteristics such as a high lift-to-drag ratio, gentle stall behavior, and good performance at various angles of attack. The airfoil demonstrates exceptional aerodynamic performance, achieving a maximum lift coefficient of 1.33 at an angle of attack of 11 degrees in an environment with a Reynolds number of 3 million. Furthermore, it boasts a coefficient of lift of 0.33 at a zero angle of attack, highlighting its efficiency in generating lift.

As illustrated in Figure 7, the lift coefficient experiences a decline when the angle of attack exceeds the 11-degree mark. This decrease in lift coefficient suggests the possibility of flow separation occurring at higher angles of attack, leading to a drop in performance. Also, the experiment was done in a 3 million Reynold number environment (marked as a circle in Figure (7)) on 24 inches (0.6096 meters) airfoil.

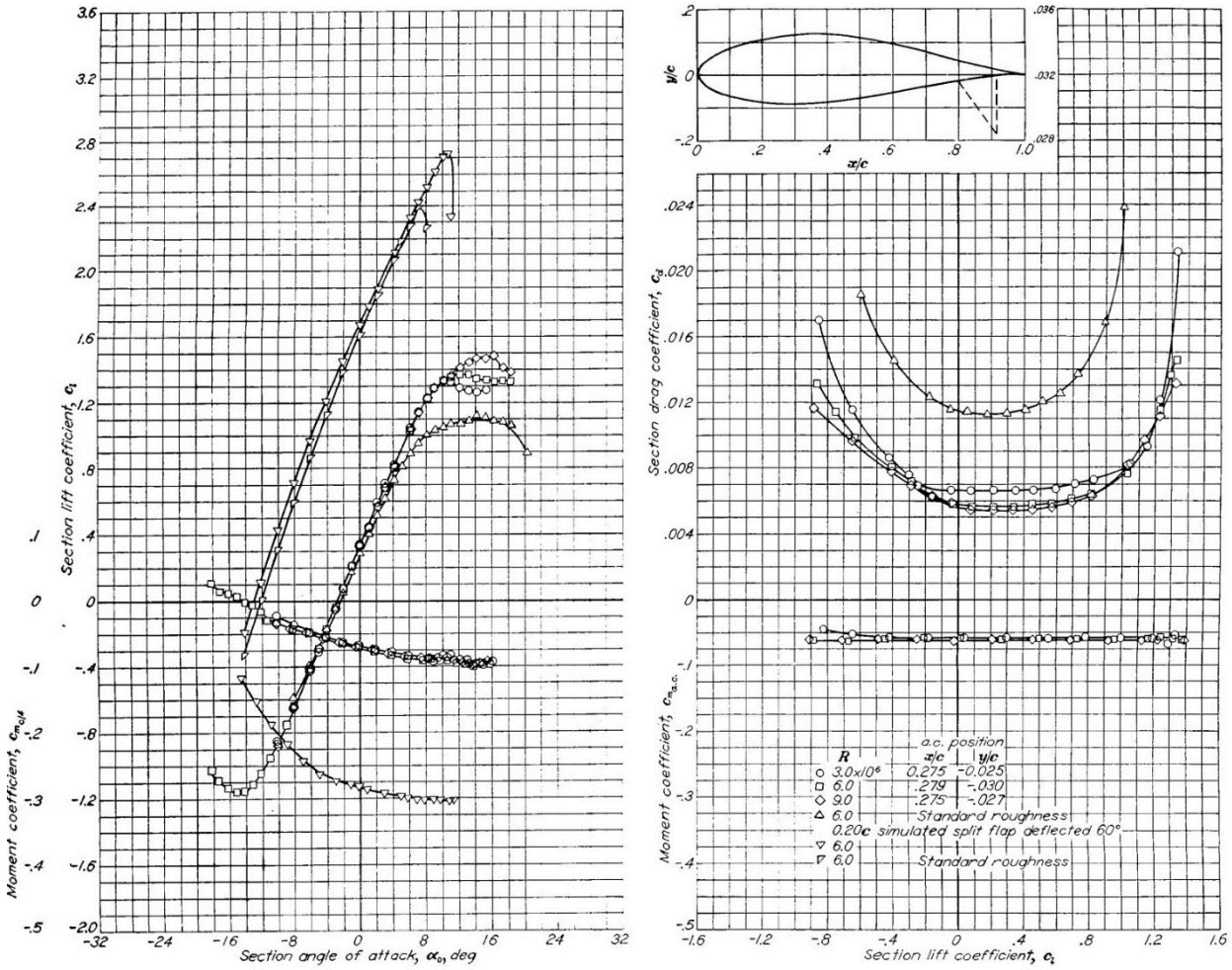

Figure 7. NACA 63(4)-421 Drag and lift table.(10)

This specific airfoil possesses a maximum thickness of 21% at 34.9% of the chord length from the leading edge. Additionally, it exhibits a maximum camber of 1.1% located at 50% of the chord. The NACA 63(4)-221 airfoil, at a 0-degree angle of attack, exhibits a coefficient of lift value of approximately 0.28, which is significantly lower compared to the NACA 634421 airfoil. This disparity in lift generation can be attributed to the airfoil's relatively lower camber value. The airfoil demonstrates peak performance (approximately 1) at a 12-degree angle of attack, maintaining nearly constant lift coefficients up to 16 degrees. Beyond this point, a gradual decrease in the lift is observed, likely resulting from the increased camber causing flow separation and turbulence.

By comparing Figure 7 and Figure 8, it can be hypothesized that an increase in the camber line of an airfoil generally leads to an increase in the amount of lift produced by the airfoil, particularly at higher angles of attack. This is because an airfoil with a more pronounced camber line will typically generate more curvature in the flow of air over its surface, resulting in a larger pressure difference between the upper and lower surfaces of the airfoil. This pressure difference produces a lifting force on the airfoil, which can be further increased by increasing the angle of attack.

However, it is important to note that there are limits to the effectiveness of increasing the camber line. At some point, increasing the camber line beyond a certain threshold will result in diminishing returns, as the airfoil may begin to experience the separation of the boundary layer or flow turbulence, which can reduce the lift generated by the airfoil and increase drag.

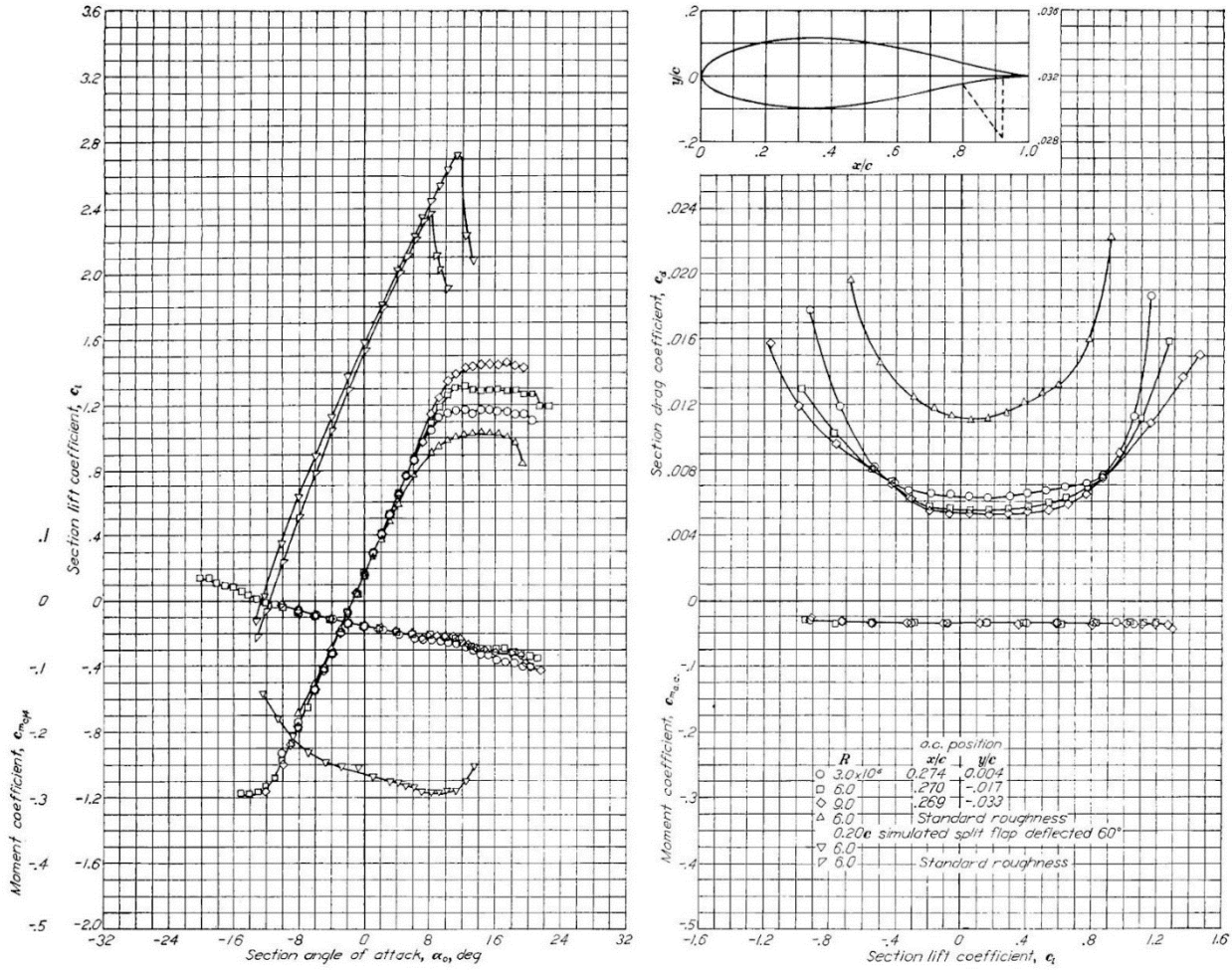

Figure 8. NACA 63(4)-221 Drag and lift coefficient table.(10)

The NACA 65(4)-421 airfoil features a maximum thickness of 21% at 39.9% chord, along with a maximum camber of 2.2% located at the 50% chord position. At a 0-degree angle of attack, the NACA 65(4)-421 airfoil outperforms its counterparts with a coefficient of lift of 0.38. Also, this particular airfoil has a very optimal maximum coefficient of lift 1.3 at 18 angles of attack although the specifications of this airfoil and the previous ones are almost identical, the location of the maximum thickness and camber differ. The previous airfoils exhibit maximum thickness at 34.8% and 34.9% chord, whereas the NACA 65(4)-421 airfoil has its maximum thickness at 39.9% chord.

Upon examining the graphical representation of these airfoils, it can be hypothesized that the more gradual increase in the frontal section of the NACA 65(4)-421 airfoil may contribute to a smoother and more attached airflow.

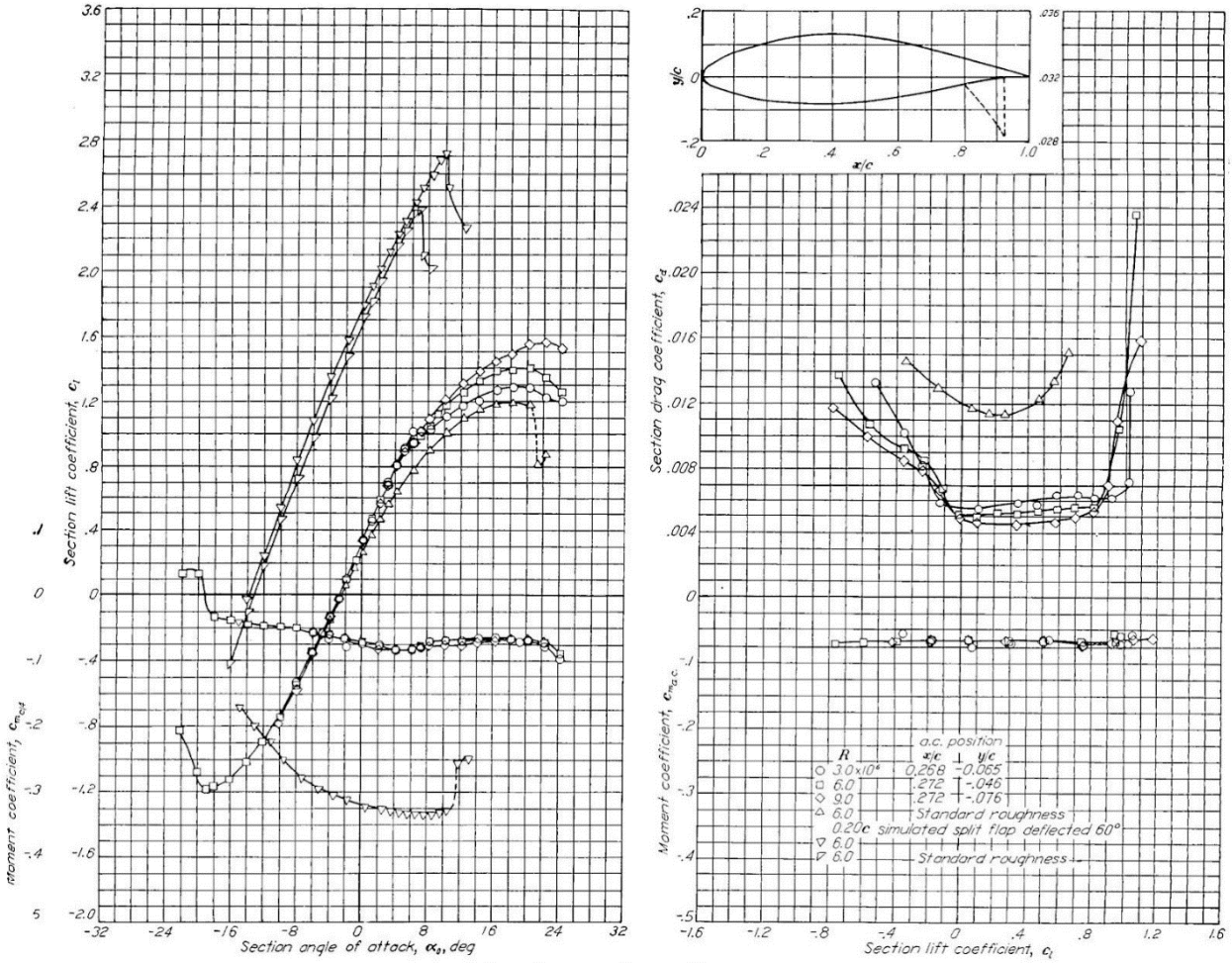

Figure 9. *NACA 65(4)-421 Drag and lift coefficient table.*(10)

The NACA 65(4)-421 a=0.5 airfoil features a maximum thickness of 21% located at 39.9% chord and a maximum camber of 3% situated at 45% chord. This particular airfoil has a 0.31 coefficient of lift at 0 angles of attack. The performance of the NACA 65(4)-421 a=0.5 airfoil may not be optimal, as it exhibits a maximum coefficient of lift of approximately 0.9 at an 8-degree angle of attack. This outcome may be attributed to the higher camber line positioned towards the front of the airfoil, in comparison to the NACA 65(4)-421 airfoil. Also, it is important to note that there are limits to the effectiveness of increasing the camber line. At some point, increasing the camber line beyond a certain threshold will result in diminishing returns, as the airfoil may begin to experience the separation of the boundary layer or flow turbulence, which can reduce the lift generated by the airfoil and increase drag.

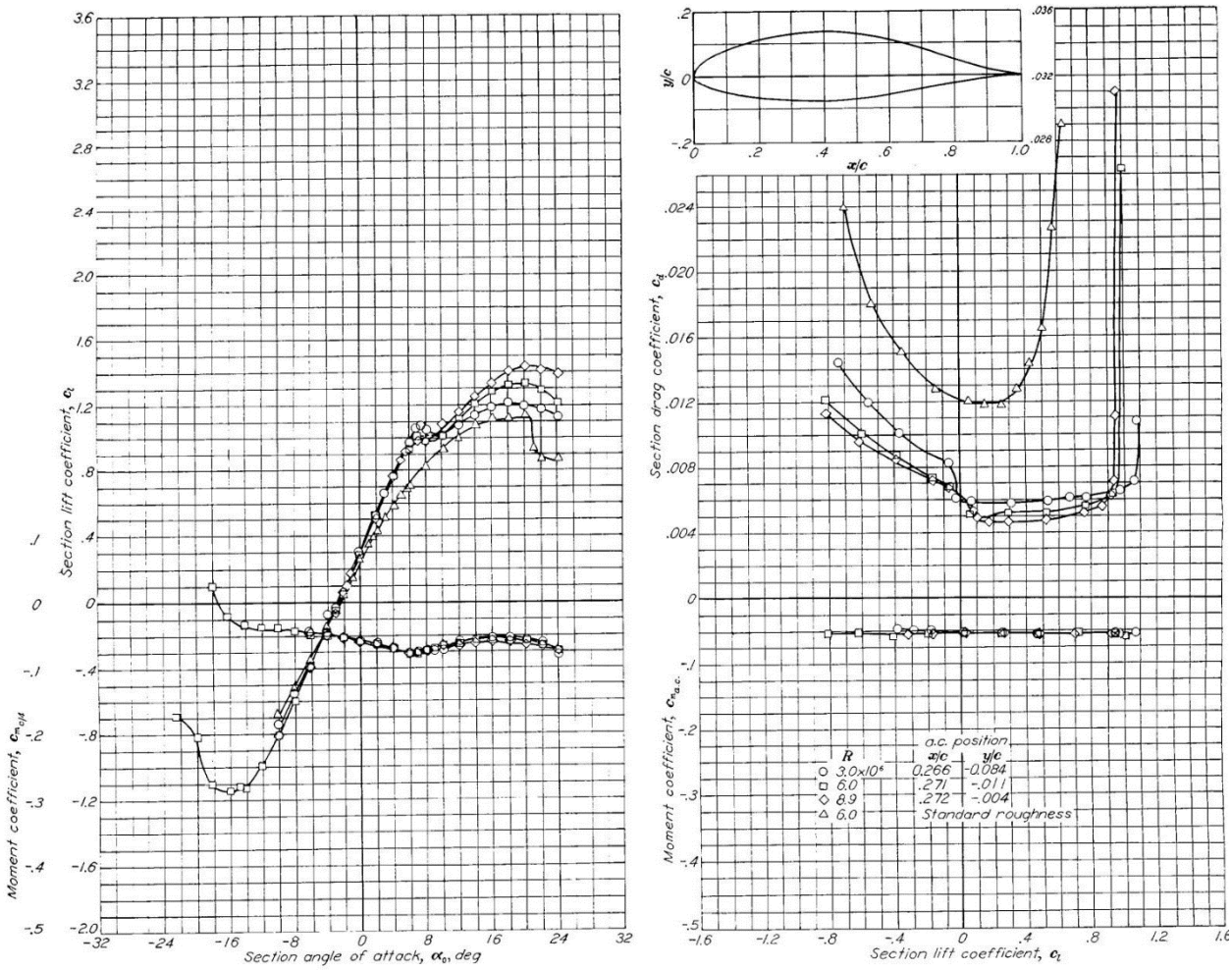

Figure 10. NACA 65(4)-421 Drag and lift coefficient table(10)

3.3 Determination of Simulation y+ value

The y+ value is a non-dimensional parameter used in computational fluid dynamics (CFD) to evaluate the quality of boundary layer meshing around an airfoil or any other surface in contact with a fluid flow. The y+ value represents the distance from the wall to the first grid point in the boundary layer, scaled by the local wall shear velocity and the fluid's kinematic viscosity.

A suitable y+ value ensures that the boundary layer mesh resolution adequately captures the critical flow phenomena near the wall, such as turbulence, skin friction, and the transition from laminar to turbulent flow.

The determination process will utilize the formula and process previously stated in section 2.2.6.

$$C_f = \frac{0.026}{Re_x^{1/7}} \quad \text{(Eq.10)}$$

Using the previous Reynold number, calculation of Cf (skin friction coefficient) is possible. Replacing the Re number in the equation Cf is now 0.003545204. Not rounding or approximating the calculated values is important since it is used in calculating very sensitive or miniature space.

$$\tau_{wall} = \frac{C_f \cdot \rho \cdot U^2}{2}$$ (Eq.11)

τ_{wall}- the shear stress at the wall

Also, by replacing all the known variables in this equation Cf, and U. The wall value is 1.882401118.

$$U_{friction} = \sqrt{\frac{\tau_{wall}}{\rho}}$$ (Eq.12)

$U_{friction}$- the friction velocity

Utilizing the previous value computation of friction velocity is possible. The friction velocity is 1.515682046

$$\Delta S = \frac{y^+ \cdot \mu}{U_{friction} \cdot \rho}$$ (Eq.13)

By rewriting equation 8 now the author can find s or the required wall size. It equals to 1.3529E-05 which means that the simulation's innermost wall height must be equal to or lower than the found value to simulate accurately.

3.4 Simulation

After choosing the airfoil design from a verified source such as the University of Illinois' UIUC Airfoil Coordinates Database. CFD (Computational Fluid Dynamics) analysis requires a systematic approach. In order to perform a successful simulation and mesh design, the following steps have been done:

Airfoil geometry: The author has Imported airfoil geometry and utilized Ansys Design modeler software. To ensure that the geometry is clean and well-defined for accurate simulation results. Draw a rectangle or other desired shape around the airfoil that encompasses the original 15x15 meter domain. The dimensions of this new domain should be large enough to minimize the influence of the boundaries on the flow around the airfoil.

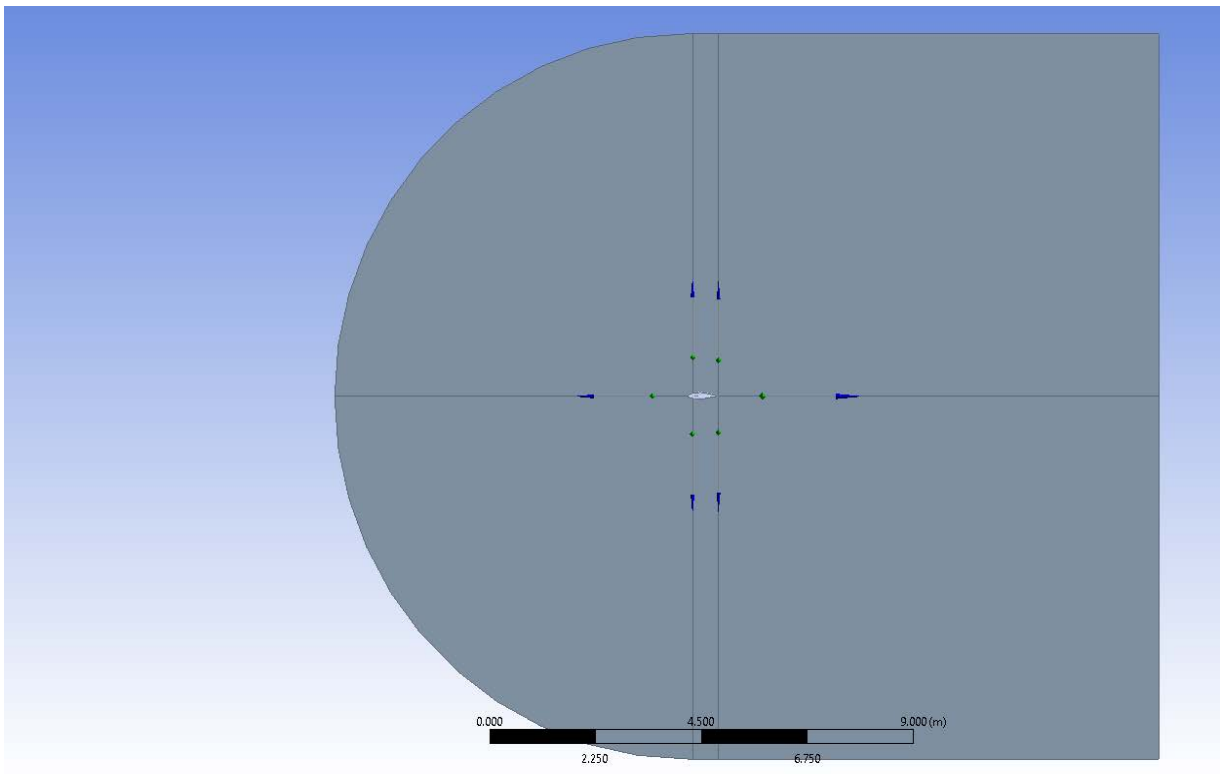

Figure 11. Geometry of airfoil and surrounding body.

Before starting the mesh simulation, the author has divided the created domain into 6 projections. Due to the complex size of the NACA 6 digits airfoil only one domain cannot provide satisfactory mesh division.

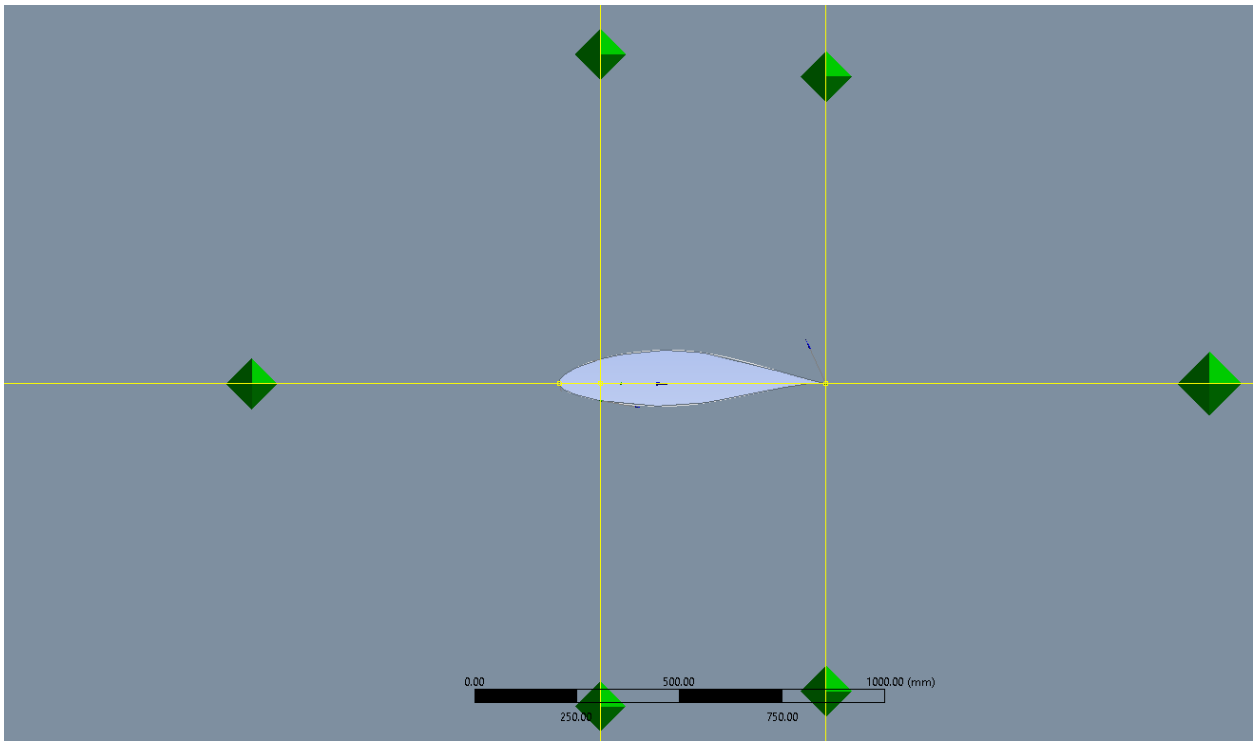

Figure 12. 6 projections on airfoil body.

Meshing: Import the airfoil geometry into a pre-processing software like ANSYS Meshing. Create a mesh around the airfoil by dividing the domain into smaller elements. A high-quality mesh will have a finer resolution near the airfoil surface and wake regions to capture boundary layer effects and flow separation accurately. A structured mesh (quad or hexahedral elements) is generally preferred for airfoil simulations. During the meshing process, y plus value has been taken into consideration. The required wall height or s has to be equal to or lower than 1.3539e-05 meters. Figure 13 and Figure 14 below illustrates how the general mesh is created for all the simulations. The irregularities occurring in the frontal lower half are negligible due to its location far away from the airfoil surface which will not have a significant impact. Meshing will be checked during the simulation process.

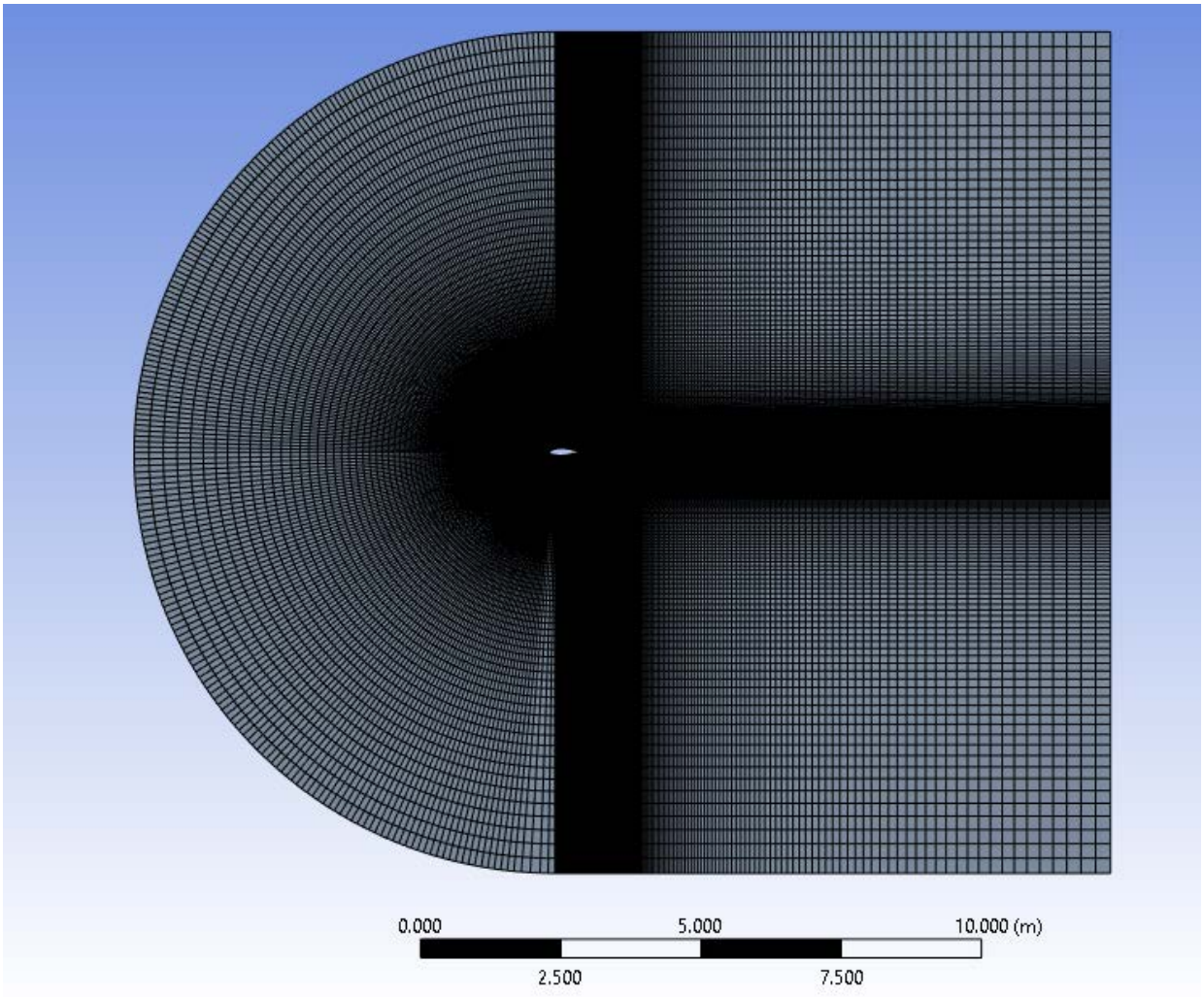

Figure 13. General mesh design

From Figure 12 6 projection can be seen more clearly. The division will help to get clear and more accurate results. Also, to accurately capture the flow behavior in the viscous sublayer and boundary layer regions, a mesh size has been decreasing around the airfoil surface. It involves defining the number of layers, growth rate, and target y+ value for the first cell height.

Care has been taken to ensure that the inner layer mesh transitions smoothly to the outer mesh and that any distorted or collapsed elements are improved upon by adjusting settings accordingly.

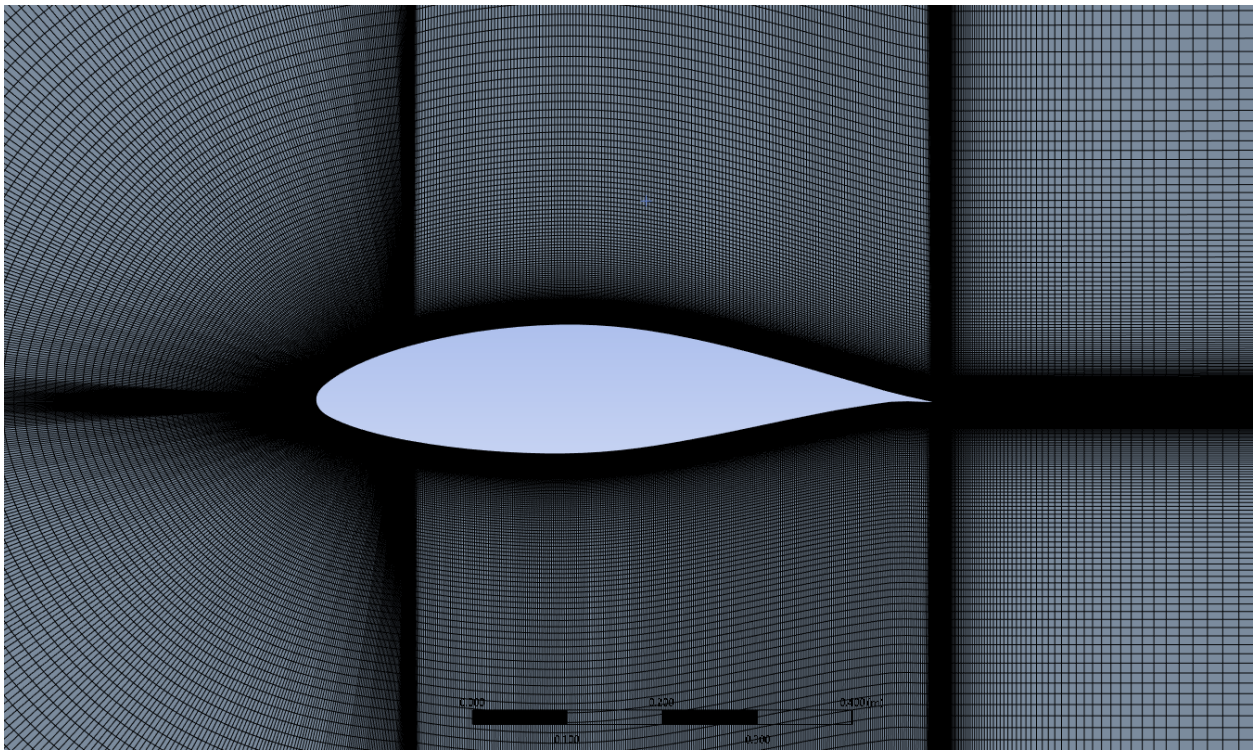

Figure 14. Close up shot of Mesh design

Boundary conditions: The inlet boundary condition is specified using the Magnitude and Direction method in the Absolute reference frame. The velocity magnitude is set to 36 m/s. The flow is considered to be subsonic, and the initial gauge pressure is set to 0 Pa. The components of flow direction in the x and y directions are given as 0 and 0, respectively. These values represent the cosine and sine of the flow angle, indicating a right angle relative to the x-axis. Also, these cosine and sine values control the angle of attack.

For turbulence modeling, the Turbulent Specification Method is set to Intensity and Viscosity Ratio. The turbulent intensity, which is a measure of the turbulence energy in the flow, is specified as 5% of the mean flow velocity. This value is a typical assumption for moderate turbulence levels in external aerodynamic simulations. The turbulent viscosity ratio is set to 10, which is a standard value used to describe the ratio between the turbulent and laminar viscosity. This value helps to determine the turbulent eddy viscosity, which is important for the turbulence model's accuracy in predicting flow separation, mixing, and other turbulent flow phenomena.

1. Inlet: Velocity or pressure-based inlet conditions
2. Outlet: Pressure or mass flow rate outlet conditions
3. Airfoil surface: No-slip wall condition

From the Figure 15 3 main body can be seen.

Property	Density	Depth	Enthalpy	Length	Pressure	Temperature	Velocity	Viscosity
Value	0.8194	1	0	1	0	262.2	36	16803E-5
Unit	Kg/m^3	m	J/kg	m	Pa	K	m/s	Kg/(m s)

Table 5. Inlet boundary conditions

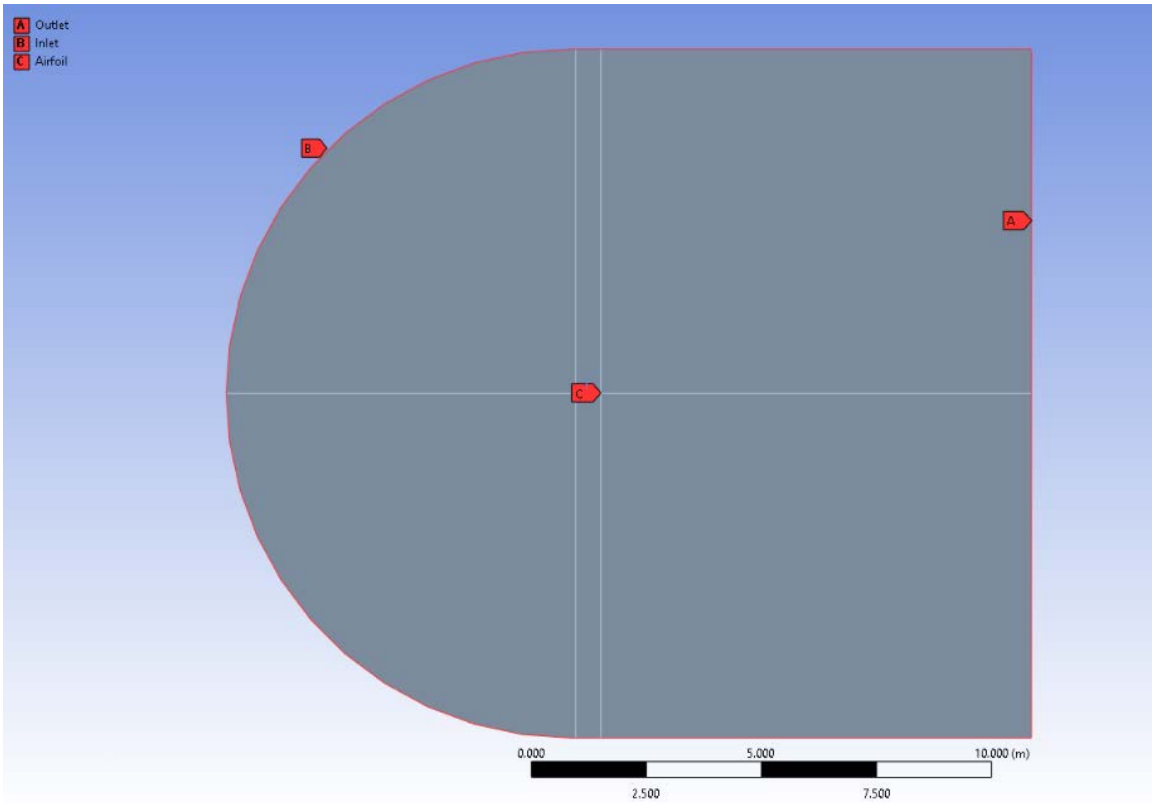

Figure 15. Inlet and Outlet on the body

Turbulence modeling: The author has chosen a suitable turbulence model based on the expected flow characteristics. Common turbulence models include Spalart-Allmaras, k-epsilon, k-omega, and Shear-Stress Transport (SST) k-omega Model. The choice of turbulence model will affect the accuracy of the results, especially in regions of flow separation and transition. Due to the Shear-Stress Transport (SST), the k-omega model exhibits superior performance in predicting adverse pressure gradient flows, flow separation, and the transition between laminar and turbulent flow regimes. It has been selected to model turbulence on the airfoils.

Solver settings: The solver settings define various parameters that influence the accuracy and stability of the simulation. In this case, the reference values for pressure profile multiplier and backflow direction specification method are set to 1 and "Normal to Boundary," respectively. The turbulent specification method is chosen as "Intensity and Viscosity Ratio," with a backflow

turbulent intensity of 5% and backflow turbulent viscosity ratio of 10. The option to build artificial walls to prevent reverse flow is set to "no." The wall boundary condition for the airfoil is set as a stationary wall with a no-slip condition, which assumes that the velocity of the fluid at the wall is zero. The wall surface roughness is set to 0, indicating a smooth surface.

The reference zone, fluid properties, and ratio of specific heats are defined, and the equations for flow and turbulence are enabled. The absolute velocity formulation is set to "True," and explicit relaxation factors for various variables, such as density, body forces, turbulent kinetic energy, specific dissipation rate, and turbulent viscosity, are provided.

The pressure-velocity coupling method is set to "Coupled," and the discretization schemes for pressure, momentum, turbulent kinetic energy, and specific dissipation rate are all set to "Second Order." These schemes improve the accuracy of the simulation compared to first-order methods.

Solution limits for absolute pressure, temperature, turbulent kinetic energy, specific dissipation rate, and turbulent viscosity ratio are defined to ensure the stability of the numerical solution and prevent unrealistic results.

3.5 Computation of Cl and Cd

To achieve accurate analysis and validate the CFD simulation methodology, the author conducted a simulation of the NACA 63(4)-421 airfoil with a chord length of 0.6096 meters. This particular airfoil was chosen due to the availability of experimental wind tunnel data, which serves as a reliable benchmark for evaluating the performance of the analytical model. The experiment was done by NACA (National Advisory Committee for Aeronautics) in a wind tunnel. The experiment was done in an environment with 3 million Reynold numbers. In order to simulate the accuracy of the analysis the author has changed the inlet velocity to 43.85 m/s. By setting the velocity to 43.85 m/s 3 million Reynold number was achieved. The objective of this preliminary simulation was to fine-tune the solver settings, turbulence models, and meshing strategies to closely match the experimental results, thus ensuring a high level of confidence in the accuracy of the CFD predictions.

The process began by carefully preparing the airfoil geometry and importing it into the CFD software. A high-quality mesh was generated, paying close attention to the boundary layer and wake regions to accurately capture flow separation and other critical flow phenomena. The turbulence model, boundary conditions, and solver settings were all selected based on the expected flow characteristics and the specific requirements of the simulation. This involved selecting appropriate values for parameters such as turbulent intensity, turbulent viscosity ratio, discretization schemes, and convergence criteria, among others.

Once the simulation was set up, it was run and the results were compared with the experimental wind tunnel data. Key performance metrics, such as lift and drag coefficients, pressure distribution, and flow visualization, were closely examined to assess the accuracy of the CFD predictions. Any discrepancies between the numerical and experimental results were carefully analyzed, and the simulation settings were iteratively refined to minimize these differences.

Having successfully validated the CFD simulation methodology for the NACA 634-421 airfoils with a 0.6096-meter chord, the author gained valuable insights into the best practices for meshing, turbulence modeling, and solver settings. These insights can now be applied to future simulations involving airfoils with a 0.65-meter chord length or other similar geometries. By following this rigorous validation process, the author has significantly increased the level of confidence in the accuracy of the CFD predictions.

4 Simulation Result and Discussion

4.1 Validation CFD Result

In this CFD simulation study, the aerodynamic performance of the NACA 63(4)-421 airfoil with a chord length of 0.6096 meters was analyzed at a Reynolds number of 3 million. The NACA 63(4)-421 airfoil features a high camber line, with a maximum camber of 2.2% located at 50% of the chord and a thickness of 21% at 34.8% of the chord. The simulation results for lift and drag coefficients at different angles of attack were compared to evaluate the airfoil's aerodynamic characteristics. The angles of attack investigated in this study were 0 degrees, 5 degrees, and 10 degrees.

Experiment designation	Variable names	Obtained values
NACA 634421 0.6096 angles: 0-degree	Coefficient of lift (cl)	0.4065709
	Coefficient of drag (cd)	0.006196347
	Ratio (cl/cd)	65.6146
NACA 634421 0.6096 angles: 5-degree	Coefficient of lift (cl)	0.7952626
	Coefficient of drag (cd)	0.006705258
	Ratio (cl/cd)	118.6028
NACA 634421 0.6096 angles: 10-degrees	Coefficient of lift (cl)	1.211808
	Coefficient of drag (cd)	0.008093275
	Ratio (cl/cd)	149.73

Table 6. CFD analysis on NACA 63(4)-421 06096 m chord data

At an angle of attack of 0 degrees, the NACA 63(4)-421 airfoils exhibited a lift coefficient (Cl) of 0.4065709 and a drag coefficient (Cd) of 0.006196347. The lift-to-drag ratio (Cl/Cd) was found to be 65.6146, indicating that the airfoil generated a moderate amount of lift with relatively low drag at this angle of attack.

When the angle of attack was increased to 5 degrees, the lift coefficient increased to 0.7952626, while the drag coefficient slightly increased to 0.006705258. The lift-to-drag ratio improved to 118.6028, suggesting that the airfoil generated more lift per unit of drag at this angle

of attack. This demonstrates the airfoil's capability to efficiently generate lift at moderate angles of attack.

At an angle of attack of 10 degrees, the lift coefficient further increased to 1.211808, indicating a significant increase in the airfoil's lifting capability. The drag coefficient also increased to 0.008093275, but the lift-to-drag ratio remained high at 149.73. This result shows that the NACA 63(4)-421 airfoil maintains a favorable balance between lift and drag even at higher angles of attack.

This validation process is crucial in building confidence in the CFD methodology and ensuring reliable predictions for aerodynamic performance. By closely matching the simulated data to the experimental results refers to values in Figure(x), the study demonstrates the effectiveness of the chosen meshing strategies, solver settings, and turbulence models in accurately capturing the flow characteristics around the NACA 63(4)-421 airfoil.

For the original wind tunnel test at an angle of attack of 0 degrees, the lift coefficient was approximately 0.35, and the drag coefficient was 0.008. In comparison, the CFD simulation results yielded a lift coefficient of 0.4065709 and a drag coefficient of 0.006196347. Despite the slight differences, the simulated data is reasonably close to the experimental results, suggesting a reliable CFD model.

At a 5-degree angle of attack, the original wind tunnel test reported a lift coefficient of 0.9 and a drag coefficient of 0.0082. The CFD simulation in this study produced a lift coefficient of 0.7952626 and a drag coefficient of 0.006705258. Once again, the simulation results show a good level of agreement with the experimental data, further validating the accuracy of the CFD model.

Finally, at a 10-degree angle of attack, the original wind tunnel test recorded a lift coefficient of 1.3 and a drag coefficient of 0.0085. The CFD simulation results for this angle of attack were a lift coefficient of 1.211808 and a drag coefficient of 0.008093275. Despite minor discrepancies, the simulated data remains in close proximity to the wind tunnel test results, providing further confidence in the validity of the CFD model.

The comparison of lift and drag coefficients between the original wind tunnel test data and the CFD simulation results for the NACA 63(4)-421 airfoil demonstrates a strong correlation between the two datasets. Although some differences may arise from the inherent limitations of the simulation capability and the imperfect conditions in the experimental environment, the overall agreement between the simulated and experimental data highlights the reliability and accuracy of the CFD model employed in this study.

The velocity contour plot obtained from the Computational Fluid Dynamics (CFD) simulation of the airfoil provides valuable insights into the flow behavior and aerodynamic characteristics refer to Figure 16. The velocity contour plot visually represents the distribution of flow velocities over the surface of the airfoil, enabling a comprehensive analysis of the fluid dynamics.

In the velocity contour plot, different velocity magnitudes are depicted using a color map. Warm colors, such as red or yellow, represent higher velocities, while cooler colors like blue or green depict lower velocities. This color mapping facilitates the identification of regions with varying flow velocities and aids in visualizing the flow interaction with the airfoil.

The velocity contour plot reveals the formation of boundary layers along the airfoil surface, where the flow velocity decreases due to viscous effects. These boundary layers are observable as regions of lower velocity in proximity to the airfoil surface. Flow separation and attachment points can also be identified from the velocity contour plot. Flow separation occurs when the flow detaches from the airfoil surface, resulting in areas of recirculation and low velocities. Examining the velocity contour plot reveals a smooth and continuous distribution of velocities over the surface of the airfoil. No regions of recirculation or areas with significantly reduced velocities are observed, indicating the absence of flow separation. This suggests that the flow remains attached to the airfoil throughout the simulated conditions.

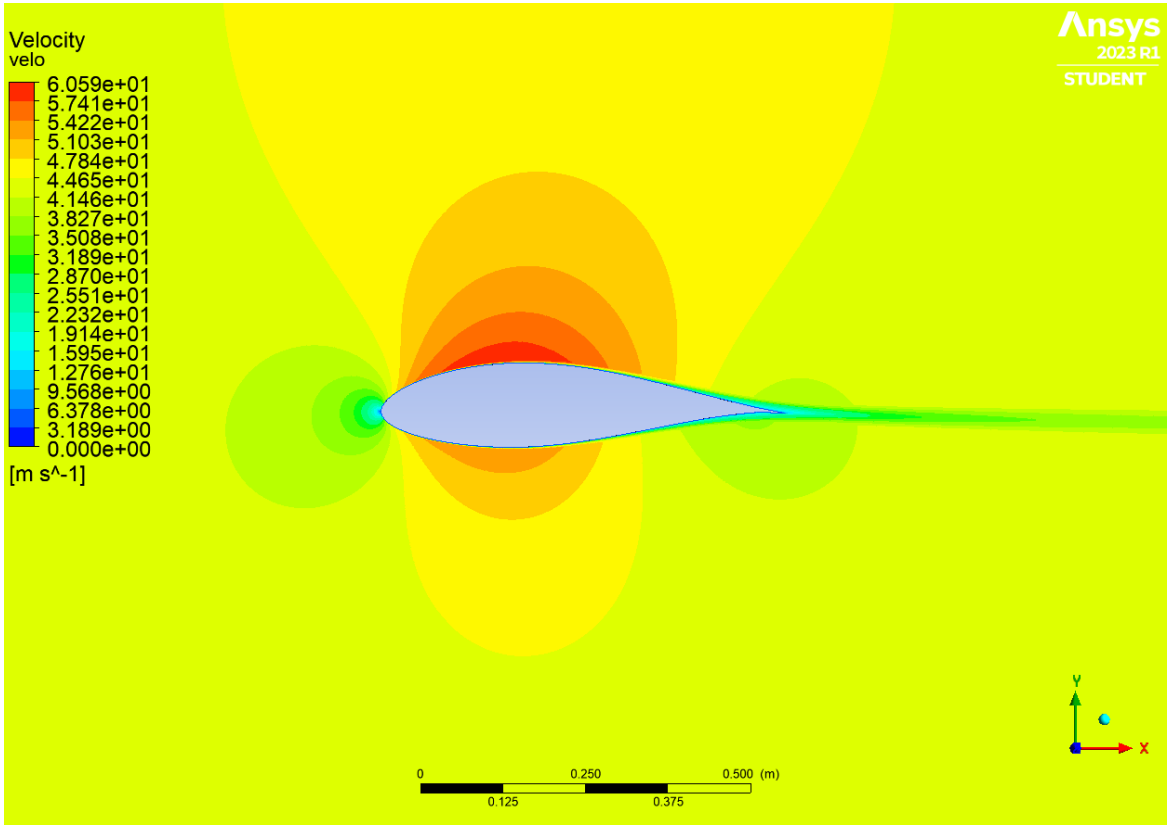

Figure 16. NACA 63(4)-421 at 0 angle of attack Velocity contour

The pressure contour plot visually represents the variation in pressure over the surface of the airfoil. The contour plot uses a color map to depict different pressure levels, with regions of higher pressure typically represented by warm colors red, orange, and yellow and regions of lower pressure represented by cooler colors light blue, blue, and green. The visualization utilized 20 different contour color mapping so that it allows for clear visualization of the pressure distribution and facilitates the identification of important flow features.

From the pressure contour plot, it can be observed that there is a favorable pressure distribution over the airfoil surface. Regions of higher pressure are generally concentrated near the leading edge of the airfoil, gradually decreasing along the surface towards the trailing edge. This pressure distribution Figure 17 indicates a positive pressure gradient, which is conducive to generating lift.

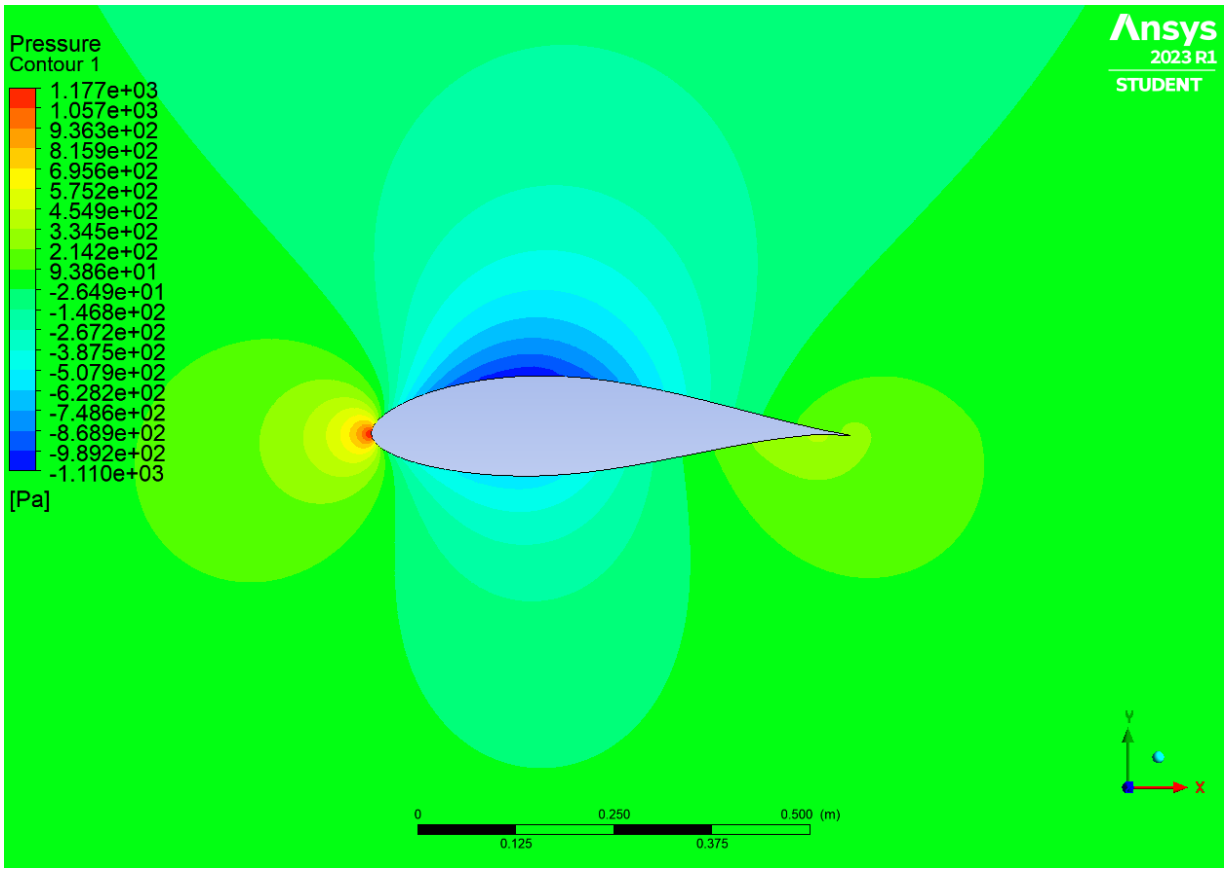

Figure 17. NACA 63(4)-421 at 0 angle of attack Pressure contour

The pressure contour plot visually represents the variation in pressure over the surface of the airfoil. The contour plot uses a color map to depict different pressure levels, with regions of higher pressure typically represented by warm colors red, orange, and yellow and regions of lower pressure represented by cooler colors light blue, blue, and green. The visualization utilized 20 different contour color mapping so that it allows for clear visualization of the pressure distribution and facilitates the identification of important flow features.

From the pressure contour plot, it can be observed that there is a favorable pressure distribution over the airfoil surface. Regions of higher pressure are generally concentrated near the leading edge of the airfoil, gradually decreasing along the surface towards the trailing edge. This pressure distribution Chart 1 and Figure 17 indicates a positive pressure gradient, which is conducive to generating lift.

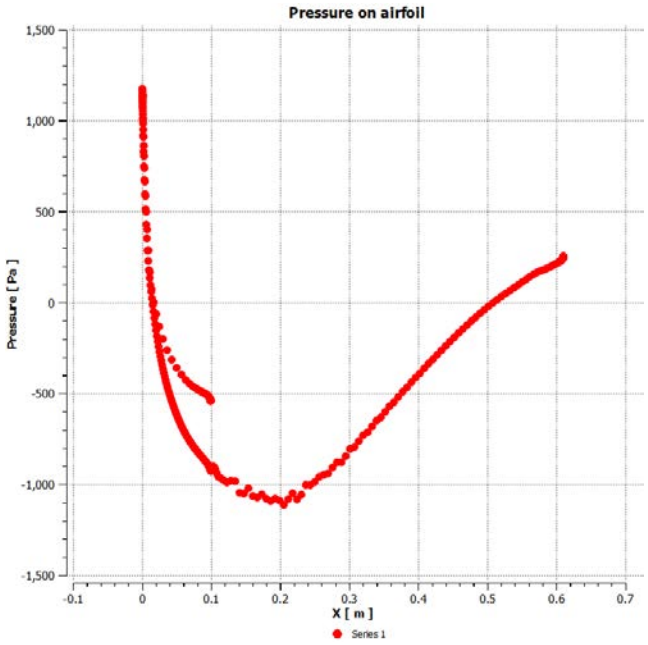

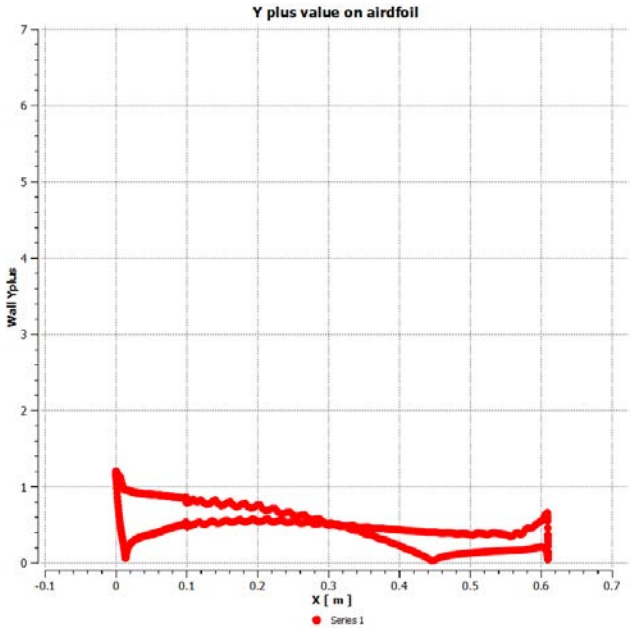

Chart 1 NACA 63(4)-421 0 pressure distribution *Chart 2 NACA 63(4)-421 0 Y + value*

A Y+ value close to one indicates refer to Chart (Y+ value) that the mesh near the wall is adequately refined, with appropriate cell size and resolution. This can help capture important flow features and minimize the errors associated with inadequate mesh resolution in the near-wall region.

4.2 General CFD simulations results

Experiments designations	Variable names	Obtained values
NACA 634221 0.65m angles: 0-degree	Coefficient of lift (cl)	0.1740
	Coefficient of drag (cd)	0.00737
	Ratio (cl/cd)	23.609
NACA 634221 0.65m angles: 5-degree	Coefficient of lift (cl)	0.6958
	Coefficient of drag (cd)	0.012
	Ratio (cl/cd)	57.983
NACA 634221 0.65m angles: 10-degree	Coefficient of lift (cl)	1.1020
	Coefficient of drag (cd)	0.0244
	Ratio (cl/cd)	45.163

Table 7. NACA 63(4)2-21 CFD simulation data

Experiments designations	Variable names	Obtained values
NACA 634421 0.65m angles: 0-degree	Coefficient of lift (cl)	0.2851
	Coefficient of drag (cd)	0.0126
	Ratio (cl/cd)	22.626
NACA 634421 0.65m angles: 5-degree	Coefficient of lift (cl)	0.8356
	Coefficient of drag (cd)	0.0138
	Ratio (cl/cd)	60.55
NACA 634421 0.65m angles: 10-degree	Coefficient of lift (cl)	1.097
	Coefficient of drag (cd)	0.028
	Ratio (cl/cd)	39.178

Table 8. NACA 63(4)-421 CFD simulation data

Experiments designations	Variable names	Obtained values
NACA 654421 0.65m angles: 0-degree	Coefficient of lift (cl)	0.2851
	Coefficient of drag (cd)	0.0126
	Ratio (cl/cd)	22.626
NACA 654421 0.65m angles: 5-degree	Coefficient of lift (cl)	0.8356
	Coefficient of drag (cd)	0.0138
	Ratio (cl/cd)	60.55
NACA 654421 0.65m angles: 10-degree	Coefficient of lift (cl)	1.097
	Coefficient of drag (cd)	0.028
	Ratio (cl/cd)	39.178

Table 9. NACA 65(4)-421 CFD simulation data

Experiments designations	Variable names	Obtained values
NACA 654421 0.65m angles: 0-degree	Coefficient of lift (cl)	0.2964
	Coefficient of drag (cd)	0.01297
	Ratio (cl/cd)	22.85
NACA 654421 0.65m angles: 5-degree	Coefficient of lift (cl)	0.7278
	Coefficient of drag (cd)	0.01996
	Ratio (cl/cd)	36.46
NACA 654421 0.65m angles: 10-degree	Coefficient of lift (cl)	0.9
	Coefficient of drag (cd)	0.037
	Ratio (cl/cd)	24.32

Table 10. NACA 65(4)-421 a5 CFD simulation data

4.2.1 NACA 63(4)-421

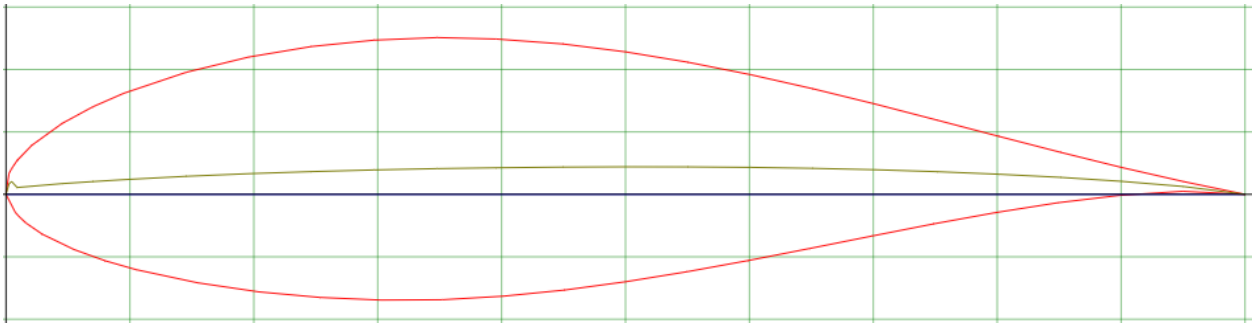

Figure 18. NACA634421 airfoil (11)

For the NACA 63(4)-421 airfoil which has a maximum thickness 21% at 34.8% chord and maximum camber at 50% chord. The NACA 63(4)-421 airfoil, characterized by a higher camber and thickness relative to NACA 63(4)-221, demonstrates an increase in lift coefficients as the angle of attack rises. At 0 degrees, the lift coefficient is 0.281018, whereas, at 5 and 10 degrees, the coefficients are 0.87384 and 1.2201, respectively. The drag coefficient also rises with the angle of attack, leading to lower lift-to-drag ratios at higher angles. The higher camber of this airfoil generates a more significant pressure difference between its upper and lower surfaces, contributing to its superior lift generation capabilities.

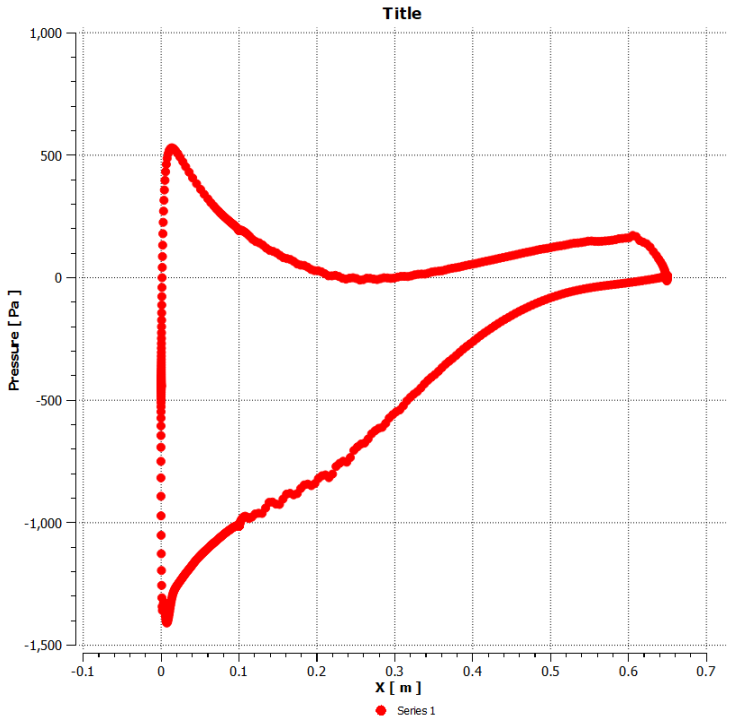

Chart 3. NACA 63(4)-421 Pressure difference 10 angle of attack

Upon examining the pressure distribution Chart 3 and Figure 19 over the airfoil, we can identify a direct correlation between the variations in pressure and the overall aerodynamic performance of the airfoil. The pressure distribution chart clearly depicts the presence of high pressure at the leading edge of the airfoil, with value of 5.303e+02. Which is then progressively decreases towards the trailing edge. On the upper surface of airfoil, a region of low pressure is observed, with value of -1.409e+3. This phenomenon is visually represented in the pressure contour through the use of warm colors, signifying areas of high pressure.

The pressure contour visualization provides a comprehensive understanding of the complex pressure patterns that occur on the airfoil surface throughout various stages of operation. By employing a wide range of color contours, the pressure contour offers detailed information on the distribution and gradients of pressure across the airfoil, enabling an in-depth analysis of its aerodynamic characteristics.

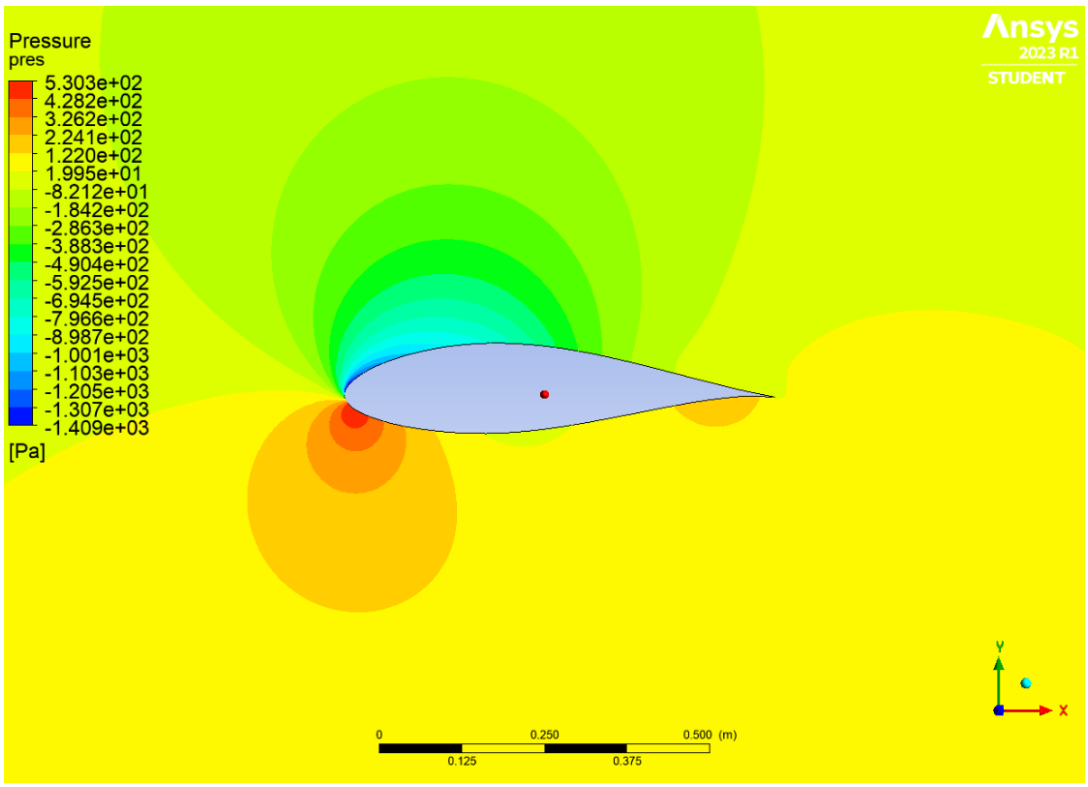

Figure 19. NACA 63(4)-421 at 10 angles of attack Pressure contour.

Furthermore, this detailed pressure analysis contributes to a more profound understanding of the lift generation process. The pressure difference between the upper and lower surfaces of the airfoil, as depicted by the contrasting warm and cool colors in the pressure contour, is responsible for creating the upward force that generates lift. Consequently, it is crucial to examine and optimize the pressure distribution patterns to enhance the airfoil's performance and achieve desired lift and drag characteristics.

4.2.2 NACA 63(4)-221

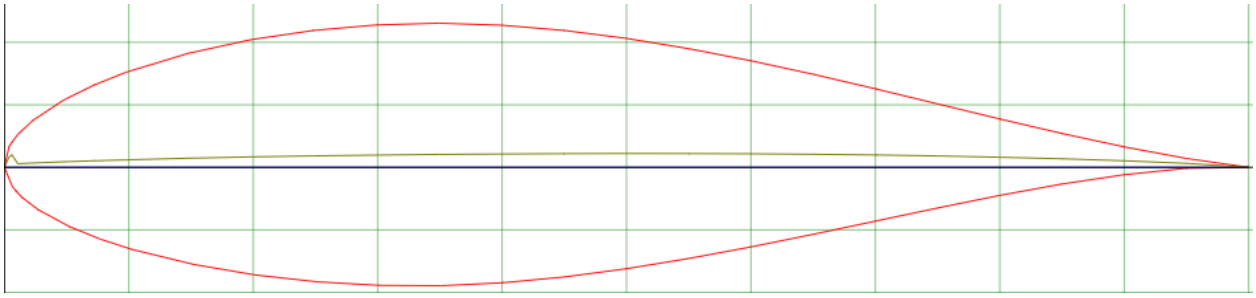

Figure 20. *NACA 63(4)-221 (12)*

The NACA 63(4)-221 airfoil, features a lower camber and thickness compared to NACA 63(4)-421 and exhibits analogous trends in lift and drag coefficients. The lift coefficient ascends from 0.1740 at 0 degrees to 1.1020 at 10 degrees. The lift-to-drag ratio, however, diminishes as the angle of attack increases, mirroring the NACA 63(4)-421 airfoil. Its lower camber results in a less pronounced pressure difference across the airfoil's surfaces, yielding lower lift coefficients compared to the NACA 63(4)-421 airfoil.

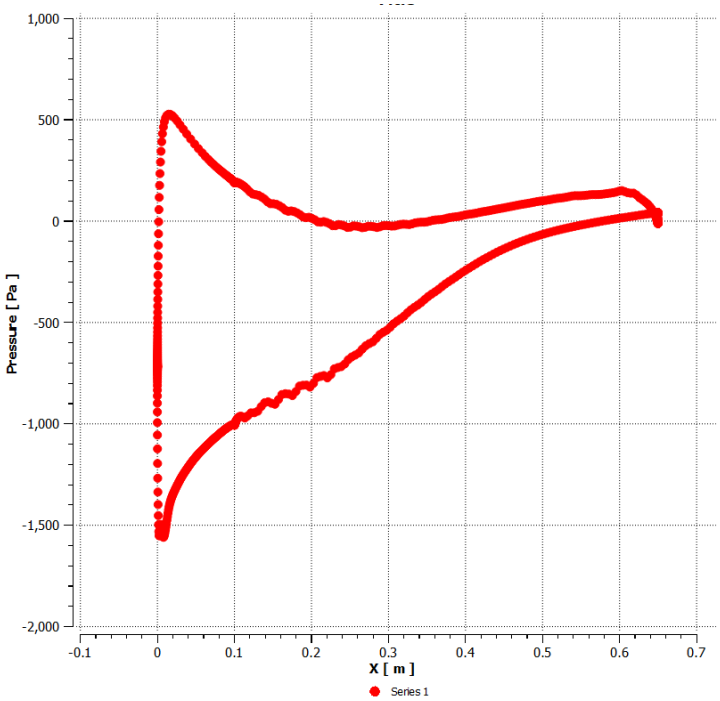

Chart 4. NACA 63(4)-221 Pressure distribution at 10 angles of attack

Upon examining the Chart 4 and Figure 21 for the NACA 63(4)-221 airfoil, the author observed high pressure at the leading edge, registering a value of 5.272e+02. This high pressure gradually subsides towards the trailing edge. On the upper surface of the airfoil, a low-pressure region is present, with a value of -1.56e+03. The pressure differential between the upper and lower surfaces of the NACA 63(4)-221 airfoil is less substantial compared to that of the NACA 63(4)-421 airfoil, which directly impacts the lift coefficient.

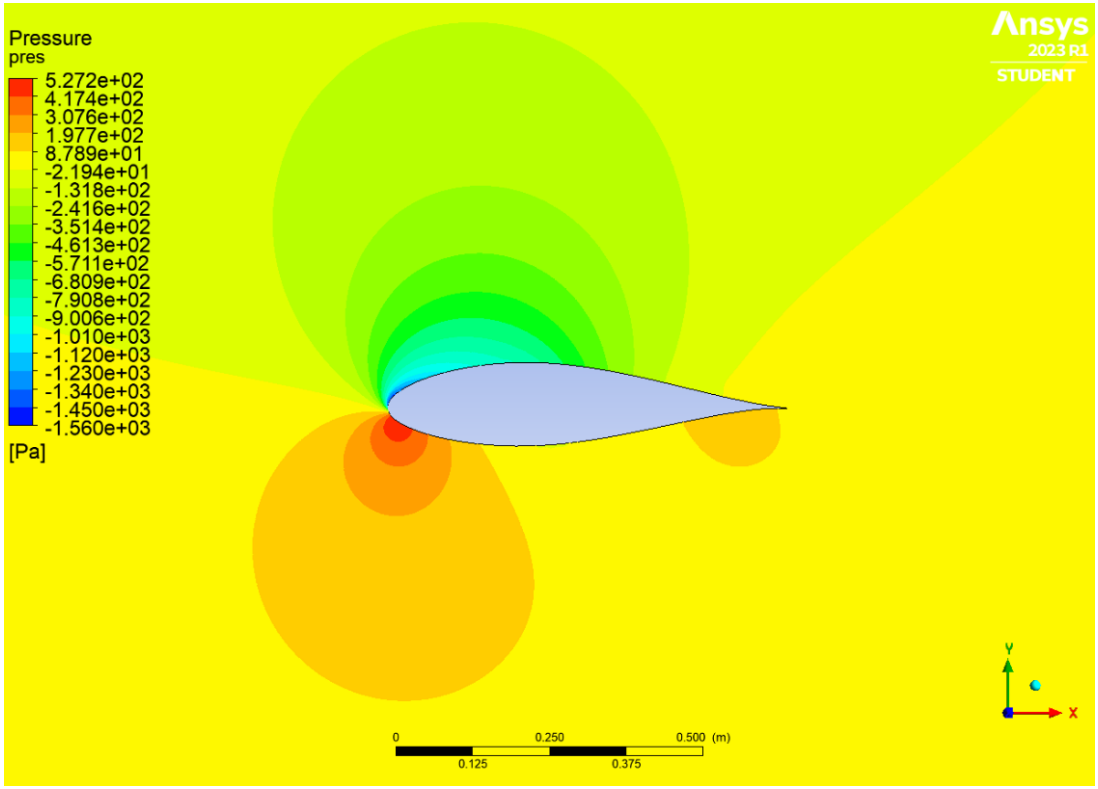

Figure 21. NACA 64(4)-221 at 10 angles of attack pressure contour

The lower camber of the NACA 63(4)-221 airfoil engenders a smaller pressure differential between its upper and lower surfaces, culminating in a lower lift coefficient when contrasted with the NACA 634-421 airfoil. The pressure differential between the upper and lower surfaces of the NACA 63(4)-221 airfoil, as depicted by the values of 5.272e+02 and -1.56e+03, is less pronounced than the corresponding pressure differential for the NACA 63(4)-421 airfoil. This smaller pressure differential results in diminished lift generation capabilities for the NACA 63(4)-221 airfoil.

4.2.3 NACA 65(4)-421

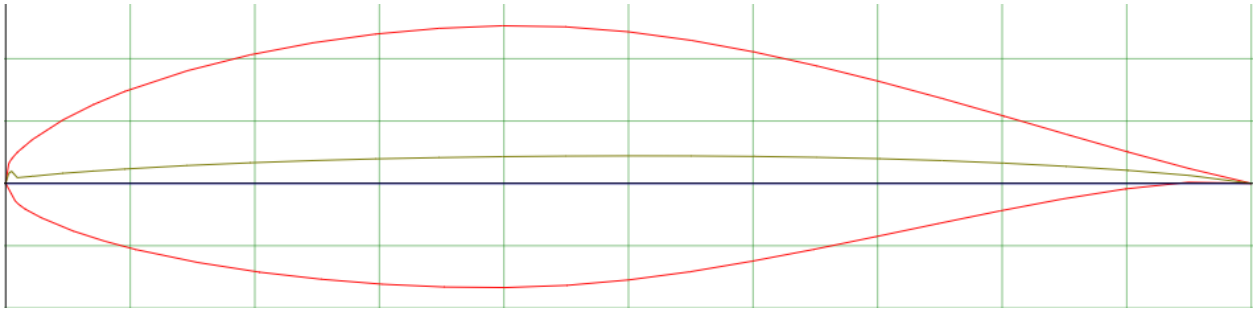

Figure 22. NACA 65(4)-421 (13)

The NACA 65(4)-421 airfoil, distinguished by a higher camber than the other airfoils and a thickness comparable to NACA 634421, exhibits an increase in lift coefficients with an escalating angle of attack, from 0.2851 at 0 degrees to 1.097 at 10 degrees. The NACA 65(4)-

421 airfoil, when analyzed at a 10-degree angle of attack, exhibits signs of flow separation. From the visual inspection of the CFD simulation results, it is evident that the flow detachment occurs on the upper surface of the airfoil, near the trailing edge. This phenomenon is indicative of a boundary layer transition from a laminar to a turbulent state, which typically occurs as the angle of attack increases.

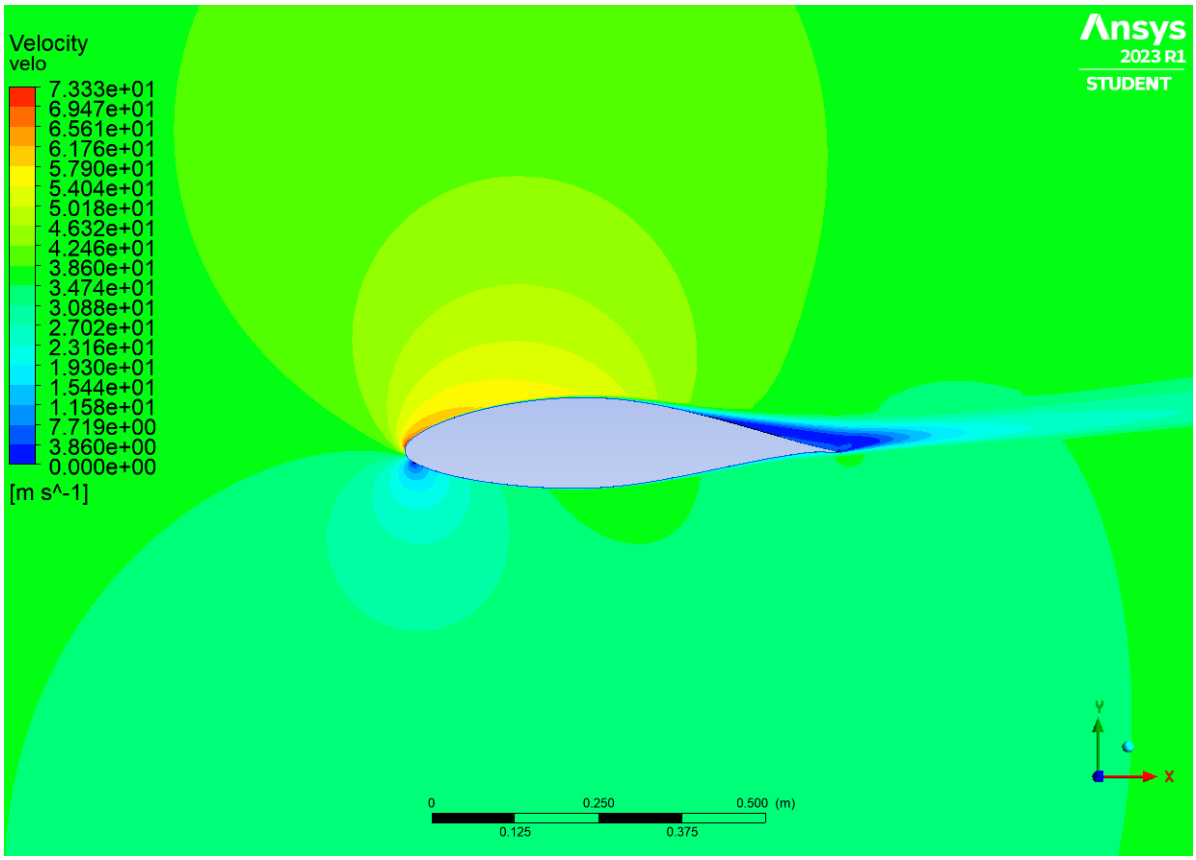

Figure 23. NACA 65(4)-421 at 10 angles of attack velocity contour flow separation

Flow separation can significantly impact the airfoil's aerodynamic performance, leading to an increase in drag and a decrease in lift. In the case of the NACA 65(4)-421 airfoil at a 10-degree angle of attack, the flow separation may be attributed to the airfoil's higher camber, causing the flow to experience a larger adverse pressure gradient as it navigates the airfoil's surface curvature. This adverse pressure gradient can result in the boundary layer losing momentum and ultimately detaching from the airfoil's surface. Also, by observing the velocity from Figure 23 flow at the trailing edge author can conclude that the flow is separated. Furthermore, by analyzing the abrupt velocity increase and decrease at the trailing edge suggest that flow is in fact turned to reverse flow. This reverse flow can lead to an increase in pressure drag, as the separated flow generates a low-pressure wake behind the airfoil. Additionally, the flow reversal can disrupt the smooth pressure recovery towards the trailing edge, resulting in a loss of lift.

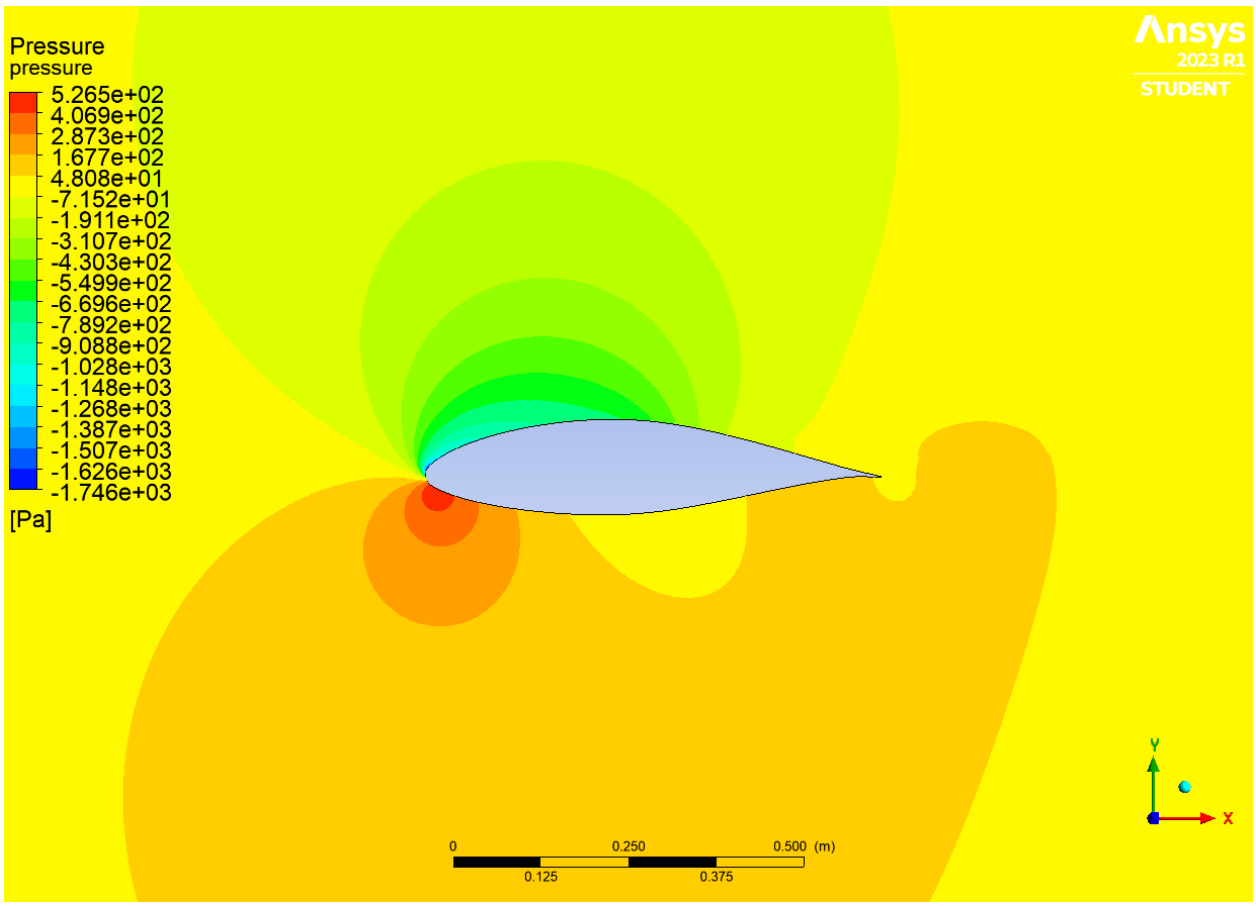

Figure 24. NACA 65(4)-421 at 10 angles of attack pressure contour flow separation)

When flow separation occurs, it influences the pressure contour by altering the pressure distribution over the airfoil's surface. Under normal conditions, the pressure gradient remains favorable, with high pressure at the leading edge gradually decreasing towards the trailing edge. However, when flow separation transpires, the pressure distribution is disrupted, and the pressure gradient may reverse, causing an increase in pressure towards the trailing edge. This reversed pressure gradient may exacerbate the flow separation, further compromising the airfoil's performance.

Figure 24 provides a visual representation of the pressure distribution over the airfoil, and flow separation can manifest as irregularities or abrupt changes in the contour patterns. In regions where flow separation occurs, the pressure contour exhibits a sudden shift from lower pressure (4.808e+1) to higher pressure (1.677e+2), indicating the presence of an adverse pressure gradient and separated flow.

4.2.4 NACA 65(4)-421-a5

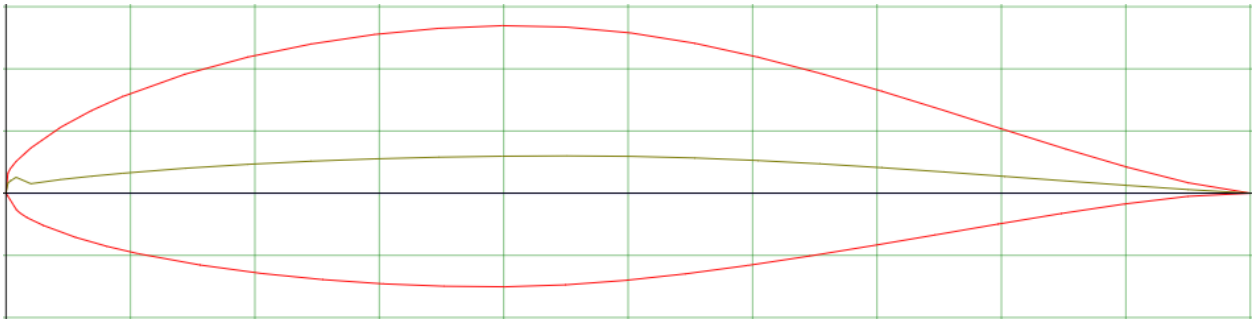

Figure 25. NACA 65(4)-421a5 (14)

Lastly, the NACA 65(4)-421 a5 airfoil, with a modified camber line compared to the standard NACA 65(4)-421 airfoil, displays an increase in lift coefficients as the angle of attack rises, from 0.2964 at 0 degrees to 0.9 at 10 degrees. The drag coefficients also escalate with the angle of attack, with the lowest lift-to-drag ratio observed at 10 degrees. The altered camber line results in a slightly different pressure distribution pattern on the airfoil's surfaces, influencing its lift generation capabilities. However, the flow detachment is visible on the airfoil's upper surface, particularly near the trailing edge. This occurrence is a result of the boundary layer transitioning from laminar to turbulent as the angle of attack increases. Moreover, flow separation can contribute to stall conditions, where the airfoil experiences a sudden decrease in lift and an increase in drag.

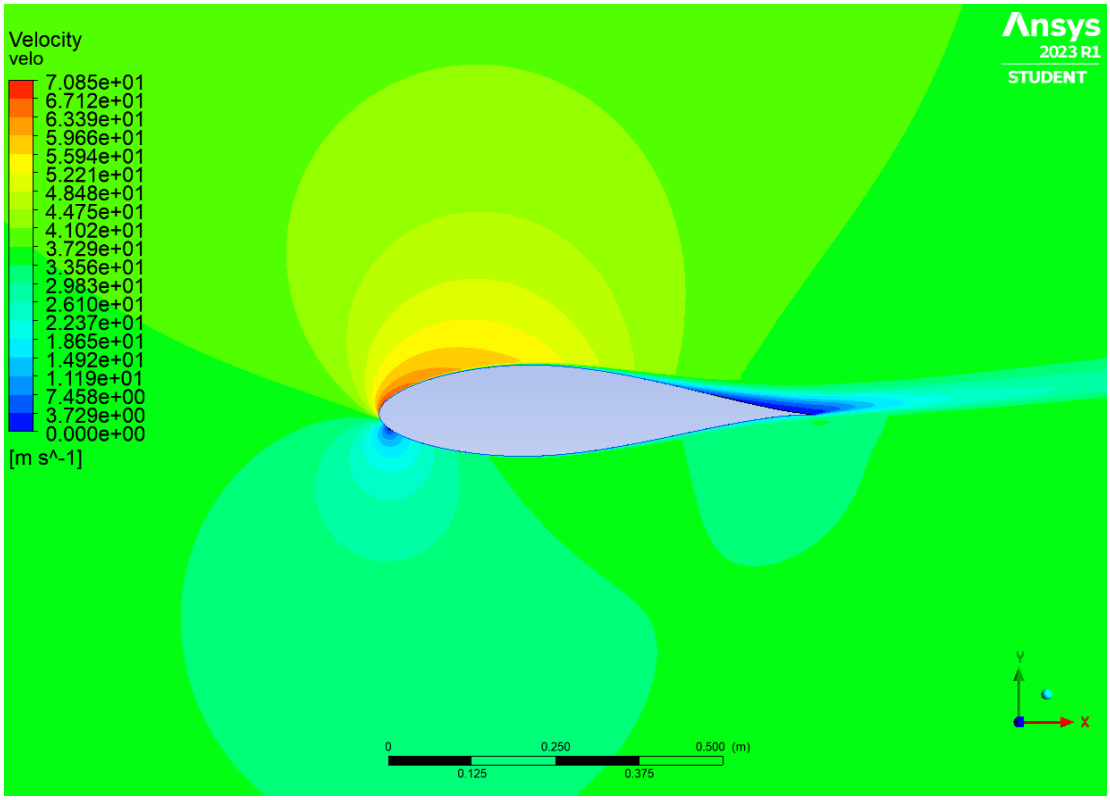

Figure 26. NACA 65(4)-421a5 at 10 angles of attack velocity contour)

Upon examining the velocity contours Figure 26, it becomes evident that regions of decreased velocity are present close to the airfoil's surface, particularly near the trailing edge. This decrease in velocity signifies the occurrence of flow separation, a phenomenon where the boundary layer loses momentum and detaches from the airfoil's surface. The flow separation disrupts the smooth pressure recovery towards the trailing edge and has a profound impact on the airfoil's aerodynamic performance.

The separated flow can lead to the formation of a low-pressure wake behind the airfoil, which, in turn, results in increased pressure drag. This drag not only affects the lift-to-drag ratio but also compromises the airfoil's overall efficiency. Furthermore, the velocity contours reveal the presence of reverse flow near the trailing edge, indicating an even more pronounced flow separation. The occurrence of reverse flow can exacerbate the airfoil's performance deterioration by causing increased turbulence and further disruption of the pressure distribution.

Of particular note is the observation that the airfoil experiences zero velocity at the trailing edge. This stagnation of velocity is a clear indication of flow separation, further confirming its occurrence and providing insight into the severity of the separation. The zero-velocity condition at the trailing edge highlights the challenges faced by the airfoil in maintaining an efficient aerodynamic performance at a 10-degree angle of attack.

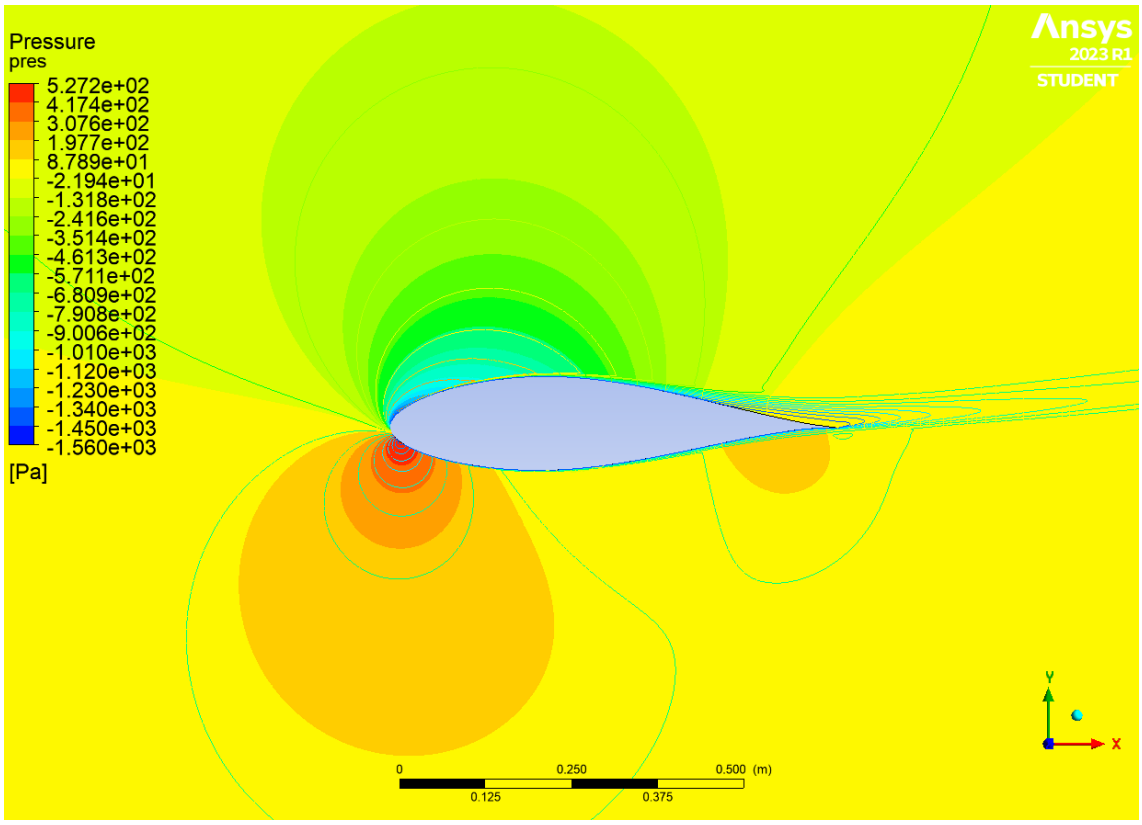

Figure 27. NACA 65(4)-421 a5 at 10 angles of attack pressure contour

The pressure contours Figure 27 also provide valuable insight into the flow separation phenomenon. In the case of the NACA 65(4)-421 airfoil at a 10-degree angle of attack, the pressure contour reveals an abrupt change in pressure distribution across the airfoil's surface. This abrupt change is indicative of an adverse pressure gradient, which causes the flow to separate from the airfoil. The separated flow disrupts the smooth pressure recovery towards the trailing edge, resulting in a loss of lift. The pressure contour also shows regions of low pressure in the wake of the airfoil, further confirming the occurrence of flow separation.

4.3 Effect of camber

The CFD simulation results for NACA 63(4)-421 and NACA 63(4)-221 airfoils with a chord length of 0.65 meters at different angles of attack (0, 5, and 10 degrees) provide valuable insights into the effects of camber on airfoil aerodynamic characteristics. Both airfoils share similar maximum thickness (21%) but differ in their maximum camber values, with NACA 63(4)-421 having 2.2% at 50% chord and NACA 634221 having 1.1% at 50% chord.

The camber has a notable impact on the lift and drag coefficients and their ratios (lift-to-drag) at various angles of attack. The lift coefficients for NACA 63(4)-421, which has a higher camber, are greater than those for NACA 63(4)-221 across all angles of attack. At a 0-degree angle of attack, the lift coefficient for NACA 63(4)-421 is 0.281018, whereas, for NACA 63(4)-221, it is 0.1740. This difference can be attributed to the higher camber in NACA 63(4)-421, which results in an increased pressure difference between the upper and lower surfaces of the airfoil.

As the angle of attack increases, the lift coefficients for both airfoils also increase. However, the lift coefficient for NACA 63(4)-421 continues to be higher than that of NACA 63(4)-221 due to its increased camber. At a 5-degree angle of attack, the lift coefficient for NACA 63(4)-421 is 0.87384, while for NACA 63(4)-221, it is 0.6958. Similarly, at a 10-degree angle of attack, the lift coefficient for NACA 63(4)-421 is 1.2201, compared to 1.1020 for NACA 63(4)-221.

The drag coefficients for both airfoils also increase with the angle of attack. However, the lift-to-drag ratios for NACA 634421 are generally higher than those for NACA 634-221, suggesting a more efficient aerodynamic performance for the airfoil with a higher camber. For instance, at a 5-degree angle of attack, the lift-to-drag ratio for NACA 63(4)-421 is 60.431, while for NACA 63(4)-221, it is 57.983.

As previously discussed, the camber line plays a crucial role in determining the velocity distribution over an airfoil's surface, which in turn affects its aerodynamic performance. A higher camber, as observed in the NACA 63(4)-421 airfoil, leads to a more pronounced curvature of the camber line. This increased curvature causes the flow to accelerate more over the upper surface of the airfoil, resulting in higher velocities and lower static pressures, according to Bernoulli's principle. Simultaneously, the flow over the lower surface experiences lower velocities and higher static pressures Figure 28.

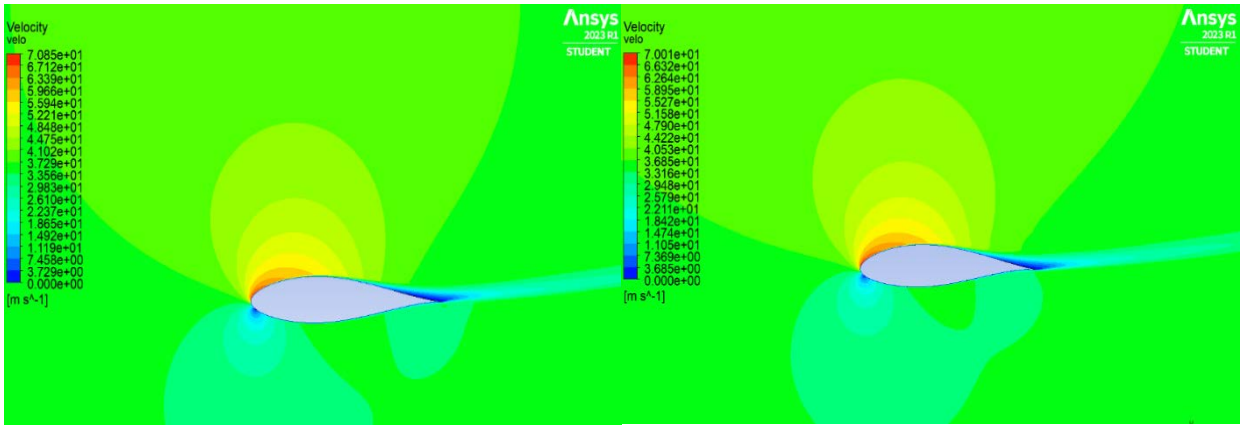

Figure 28. NACA 63(4)-221 and NACA 63(4)-421 velocity contour

Bernoulli's principle, which relates the pressure, velocity, and elevation of a fluid within a flow, states that as the velocity of a fluid increases, its pressure decreases, and vice versa. Consequently, the pressure difference between the upper and lower surfaces of the airfoil generates lift, with the more significant pressure difference in the NACA 63(4)-421 airfoil leading to higher lift coefficients compared to the NACA 63(4)-221 airfoil Figure 29.

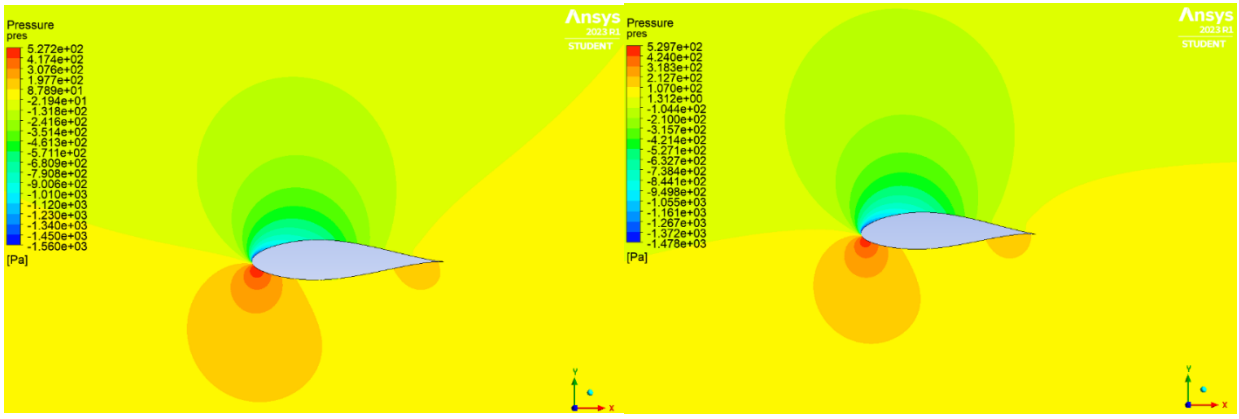

Figure 29. NACA 63(4)-221 and NACA 63(4)-421 pressure contour

The consistently higher lift coefficients for NACA 634-421, as compared to NACA 634-221, demonstrate the positive effect of increased camber on lift generation. This enhanced lift production can be attributed to the altered flow field around the airfoil due to the higher camber,

which, in accordance with Bernoulli's principle, results in more significant pressure differences between the upper and lower surfaces Chart 5.

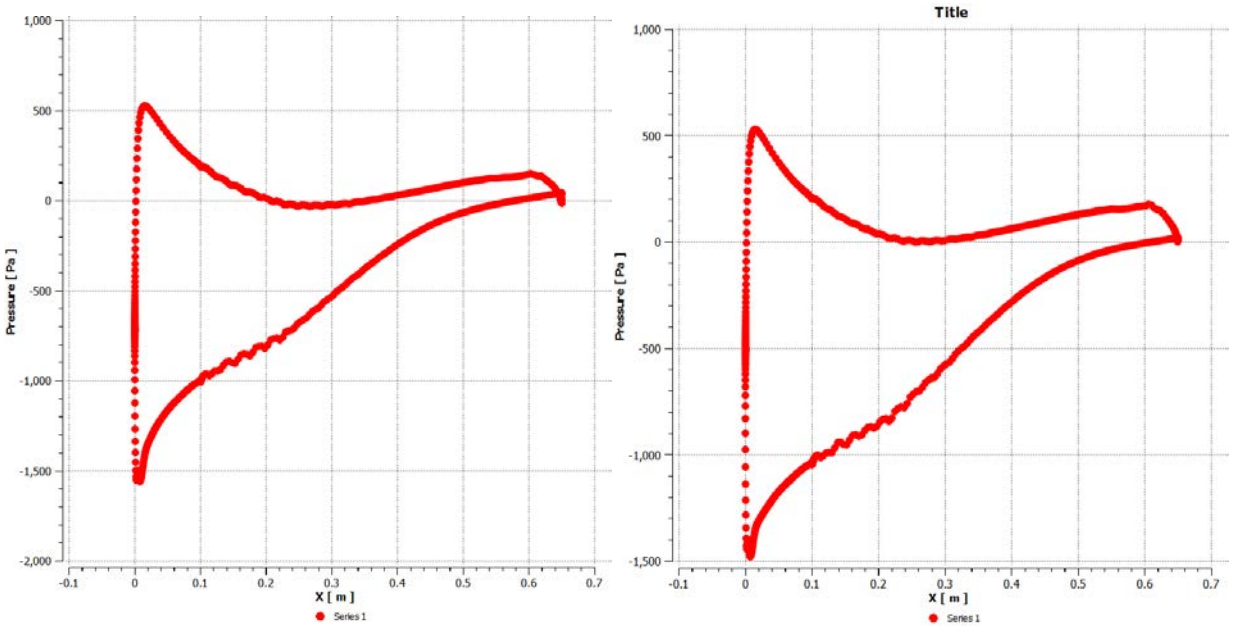

Chart 5. NACA 63(4)-221 and NACA 63(4)-421 pressure difference at 10 angles of attack

The camber line of an airfoil plays a significant role in influencing its aerodynamic characteristics, particularly the lift generated. The camber line is the curve connecting the midpoints of the upper and lower surfaces of the airfoil, representing the mean line or the average shape of the airfoil. An airfoil with a higher camber has a more pronounced curvature in the camber line, while a lower camber airfoil has a flatter camber line.

The influence of the camber line can be seen through the following aspects:

Pressure distribution: A higher camber in the airfoil alters the pressure distribution on the upper and lower surfaces. The increased curvature causes the flow to accelerate more over the upper surface, leading to a lower pressure area, while the pressure on the lower surface increases refers in Figure 31. This results in a greater pressure difference between the two surfaces, which generates more lift.

Angle of zero lift: The angle of zero lift is the angle of attack at which the airfoil generates no lift. A cambered airfoil typically has a negative angle of zero lift, whereas a symmetric airfoil has an angle of zero lift equal to zero degrees. This means that a cambered airfoil can generate lift at smaller angles of attack compared to symmetric airfoils, improving efficiency at low angles of attack

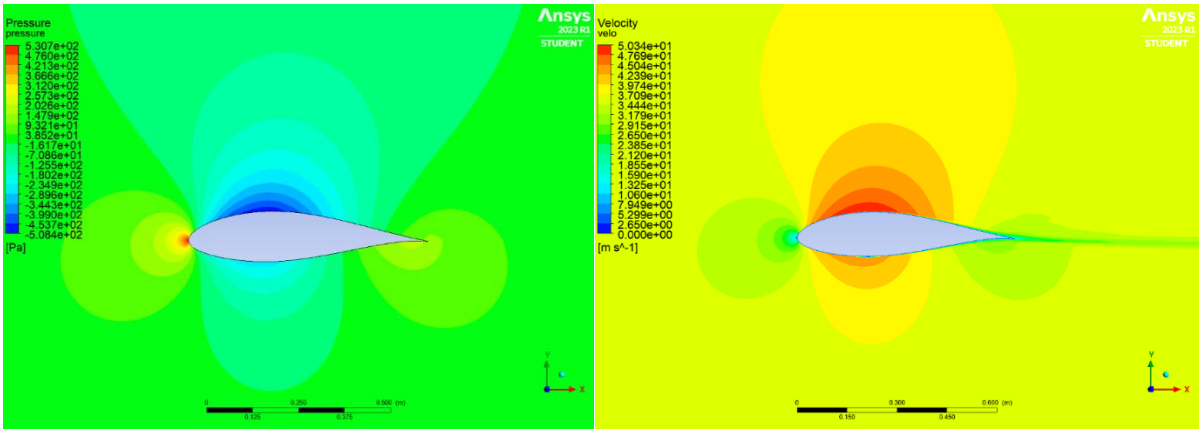

Figure 30. NACA 63(4)-421 a0 pressure contour Figure 31. NACA 63(4)-421 a0 velocity contour

Drag: The camber line can also impact the drag generated by the airfoil. A higher camber can increase the airfoil's overall curvature, which may result in an increase in form drag due to the larger surface area exposed to the airflow. However, the lift-to-drag ratio might still be higher for a cambered airfoil if the increase in lift outweighs the increase in drag, leading to better aerodynamic efficiency.

4.4 Selection of airfoil.

Considering the minimal required coefficient of lift (1.065) and the importance of a high lift-to-drag ratio for a heavy-lift drone, let's examine the airfoil options:

NACA 63(4)-421:

- 5-degree angle of attack: Lift coefficient of 0.87384 and lift-to-drag ratio of 60.431
- 10-degree angles of attack: Lift coefficient of 1.2201 and lift-to-drag ratio of 47.28

NACA 63(4)-221:

- 5-degree angle of attack: Lift coefficient of 0.6958 and lift-to-drag ratio of 57.983
- 10-degree angles of attack: Lift coefficient of 1.1020 and lift-to-drag ratio of 45.163

Based on the requirement of a minimum lift coefficient of 1.065, the airfoils must be analyzed at a 10-degree angle of attack, as the lift coefficients at a 5-degree angle of attack are lower than the required value.

Comparing the lift-to-drag ratios at a 10-degree angle of attack, the NACA 63(4)-421 airfoil has a higher lift-to-drag ratio (47.28) than the NACA 63(4)-221 airfoil (45.163). This indicates that the NACA 63(4)-421 airfoil would provide better lift generation with minimal drag penalties, which is crucial for a heavy-lift drone's efficiency and endurance. Therefore, the NACA 63(4)-421 airfoil appears to be the most suitable choice based on the given criteria.

5 Concluson

In summary, the design and selection of an airfoil for a heavy-lifting unmanned aerial vehicle (UAV) with a maximum take-off weight of 450 kg and an operating altitude of 4000 meters is a critical and intricate process. The aerodynamic efficiency and performance of the UAV are significantly influenced by the chosen airfoil. Consequently, it is imperative to carry out a comprehensive analysis of various airfoil geometries, examining their lift and drag characteristics, as well as their behavior under a wide range of angles of attack.

After thorough computational fluid dynamics (CFD) simulations, the NACA 63(4)-421 airfoil emerged as the most suitable choice for this heavy-lifting UAV. At an angle of attack of 10 degrees, the NACA 63(4)-421 airfoil met the required coefficient of lift, demonstrating its ability to generate sufficient lift for the UAV's specific mission requirements.

It is, however, essential to recognize the potential limitations and errors associated with the CFD simulations. Due to constraints on computational resources, the y-plus value utilized in the simulations was exceptionally low, which might have affected the accuracy of the results. Despite these limitations, the selection of the NACA 63(4)-421 airfoil has laid a solid foundation for the UAV's aerodynamic design.

To further enhance the airfoil design and validation process, it is strongly recommended to perform wind tunnel testing to obtain experimental data that can be utilized to validate and refine the CFD simulations. This approach will offer a more robust understanding of the NACA 63(4)-421 airfoil's performance characteristics under real-world conditions. Moreover, adopting more sophisticated simulation software with greater computational capabilities would enable a more accurate representation of flow physics and boundary layer behavior, potentially leading to the selection of an even more optimized airfoil for the heavy-lifting UAV.

In addition, continuous research and development efforts should be made to explore innovative airfoil shapes and materials, which can further improve the UAV's performance, efficiency, and reliability. Collaboration between academic institutions, research organizations, and industry partners can contribute to the advancement of airfoil design methodologies and the development of cutting-edge UAV technologies.

In conclusion, the selection of the NACA 63(4)-421 airfoil as the optimal choice for the heavy-lifting UAV has proven to be a significant milestone in the development process. By incorporating advanced design techniques, rigorous validation methods, and continuous research efforts, it is possible to develop a high-performing, efficient, and reliable UAV capable of meeting the demands of a wide range of applications, from heavy-lifting tasks to reconnaissance missions in both civilian and defense domains.

6 Reference

1. Papageorgiou A. Design Optimization of Unmanned Aerial Vehicles : A System of Systems Approach. Linköping Studies in Science and Technology. Dissertations NV - 2018. 2019.
2. Cistriani IL. Falco UAV Low Reynolds Airfoil Design and Testing at Galileo Avionica. Nato. 2007;
3. Airelectronics. Flying wing UAV. UAV X8 Flying Wing.
4. Edi P, Yusoff N, Yazid AA. The design improvement of airfoil for flying wing UAV. WSEAS Trans Appl Theor Mech. 2008;
5. Marqués P. Advanced UAV aerodynamics, flight stability and control: An introduction. Advanced UAV Aerodynamics, Flight Stability and Control: Novel Concepts, Theory and Applications. 2016.
6. Kundu P, Cohen I, Dowling D. Fluid Mechanics. Fluid Mechanics. 2012.
7. Sadraey MH. Design of Unmanned Aerial Systems. Design of Unmanned Aerial Systems. 2020.
8. White FM. Fluid Mechanics seventh edition by Frank M. White. Power. 2011.
9. NASA. Air Viscosity. In: Glenn Research Center [Internet]. Available from: https://www.grc.nasa.gov/www/BGH/viscosity.html
10. AID. Airfoil Database. Airfoil Investigation Database. 2016.
11. Airfoil Tools. NACA 63(4)-421 [Internet]. Airfoil Investigation Database. Available from: http://airfoiltools.com/airfoil/details?airfoil=naca634421-il
12. Airfoil Tools. NACA 63(4)-221 [Internet]. Airfoil Investigation Database. Available from: http://airfoiltools.com/airfoil/details?airfoil=naca644221-il
13. Airfoil Tools. NACA 65(4)-421 [Internet]. Airfoil Investigation Database. Available from: http://airfoiltools.com/airfoil/details?airfoil=naca654421-il
14. Airfoil Tools. NACA 65(4)-421 a5 [Internet]. Airfoil Investigation Database. Available from: http://airfoiltools.com/airfoil/details?airfoil=naca654421a05-il